aerospace

MDPI

Article

Numerical Simulations of Spray Combustion in Jet Engines

Arvid Åkerblom, Francesco Pignatelli and Christer Fureby *

Department of Energy Sciences, Lund University, P.O. Box 118, SE 221-00 Lund, Sweden
* Correspondence: christer.fureby@energy.lth.se

Abstract: The aviation sector is facing a massive change in terms of replacing the currently used fossil jet fuels (Jet A, JP5, etc.) with non-fossil jet fuels from sustainable feedstocks. This involves several challenges and, among them, we have the fundamental issue of current jet engines being developed for the existing fossil jet fuels. To facilitate such a transformation, we need to investigate the sensitivity of jet engines to other fuels, having a wider range of thermophysical specifications. The combustion process is particularly important and difficult to characterize with respect to fuel characteristics. In this study, we examine premixed and pre-vaporized combustion of dodecane, Jet A, and a synthetic test fuel, C1, based on the alcohol-to-jet (ATJ) certified pathway behind an equilateral bluff-body flameholder, spray combustion of Jet A and C1 in a laboratory combustor, and spray combustion of Jet A and C1 in a single-sector model of a helicopter engine by means of numerical simulations. A finite rate chemistry (FRC) large eddy simulation (LES) approach is adopted and used together with small comprehensive reaction mechanisms of around 300 reversible reactions. Comparison with experimental data is performed for the bluff-body flameholder and laboratory combustor configurations. Good agreement is generally observed, and small to marginal differences in combustion behavior are observed between the different fuels.

Keywords: large eddy simulation; spray combustion; fossil and non-fossil fuels; SAF; validation and flow elucidation

Citation: Åkerblom, A.; Pignatelli, F.; Fureby, C. Numerical Simulations of Spray Combustion in Jet Engines. *Aerospace* **2022**, *9*, 838. https://doi.org/10.3390/aerospace9120838

Academic Editor: Eugenio Giacomazzi

Received: 4 November 2022
Accepted: 9 December 2022
Published: 16 December 2022

1. Introduction and Background

During the last decades, the aviation sector has relied heavily on turbofan and turbojet engines for military, civilian, and commercial aircraft. Turboshaft engines, which are similar to turbojet engines in design but produce shaft power rather than thrust, are typically used in helicopters. The main drawback of turbofan, turbojet, and turboshaft engines is that they consume fossil jet fuel, which is in limited supply, and emit emissions, such as CO_2, soot, NO_X, and condensation trails (contrails), composed of water in the form of ice crystals. CO_2, soot, and NO_X are harmful to the environment [1], whereas the contrails affect cloud formation in the Earth's atmosphere, influencing the atmospheric temperature and climate mainly by radiative forcing [2]. As reported by Lee et al. [3], between 2000 and 2018, aviation has consumed ~2% of the fossil fuel burnt globally, representing ~12% of the fuel consumption in the transportation sector, and emitted ~3% of the total CO_2 emissions, which corresponds to ~5% of the global warming as a result of indirect effects such as contrails. Therefore, during the last decades, significant efforts have been directed towards developing sustainable aviation fuels (SAF) for aeroengines to reduce emissions and global warming effects.

Nowadays, engines are developed based on the existence of kerosene-grade jet fuels. Kerosene is a flammable liquid mixture of petroleum-based hydrocarbons produced by the distillation of crude oil, mixed with other compounds to achieve suitable qualities, having the average molecular formula of $C_{12}H_{23}$, with carbon numbers between 8 and 16. Compared to gasoline, which is another petroleum-based hydrocarbon mixture with the average molecular formula C_8H_{18}, kerosene has a lower freezing point, higher flash point, and lower viscosity, and is also cheaper to produce. Kerosene usually contains

specific additives, such as metal deactivators, corrosion inhibitors, icing inhibitors, and static dissipater additives. Jet fuels are well defined by standards, e.g., [4], defining the thermophysical property ranges of density, viscosity, vapor pressure, energy content, etc., and are required to include between 8 and 25 vol % aromatics for elastomer swelling. The jet fuel specifications are, at the same time, loose enough that notable compositional variations exist between the most common civilian jet fuels, Jet A and Jet A-1, and the most common military jet fuels, JP5 and JP8, according to, e.g., [5].

During the last decade, SAF or bio jet fuels have been recognized as an alternative short- to medium-term solution to kerosene-based jet fuels from crude oil to address climate change by reduction in greenhouse gas emissions from the aviation sector and to ensure security of supply at affordable prices, e.g., [6–8]. The technical feasibility of SAF is proven when used as drop-in fuel in fossil kerosene, shown in engine tests and flights with up to 50% sustainable jet fuel, e.g., [6]. A wide variety of feedstocks, chemical conversion technologies, and sustainable jet fuels are currently considered [9,10] and evaluated against the ASTM standard [4]. According to ICAO, as of October 2021, there are currently nine ASTM-approved pathways for SAF [11], all resulting in different fuels that are within the ASTM or MIL standards for Jet A, Jet A-1, JP5, or JP8.

Set against this background, we, here, present finite rate chemistry (FRC) large eddy simulations (LES) of fossil Jet A and n-dodecane (an often used surrogate jet fuel) and a non-fossil test fuel, C1 [12], representing the emerging class of SAFs. The majority of the simulations are performed on spray flames, where the liquid spray is modeled using a Lagrangian formulation based on the discrete droplet model (DDM). The objective of this study is to examine the sensitivity of combustion to different fossil and non-fossil jet fuels and to further validate the numerical simulation models against experimental data when available. Experimental studies exploring the sensitivity of combustion to non-fossil fuels are in short supply and, hence, the validation part has been made mainly using fossil fuels. The paper is organized as follows: first, we provide an overview of the computational and numerical methodologies used; then, we describe in more detail different fossil and non-fossil fuels and how the combustion of these fuels can be represented by different chemical reaction mechanisms. After this, we present results for different cases: a premixed equilateral triangular bluff-body stabilized flame, a generic experimental gas turbine spray combustor, and a single-sector model of a full helicopter engine. This suite of cases is selected to demonstrate that FRC-LES modeling can successfully be applied to a range of experimental and engineering combustor cases.

2. Computational Methodology

The computational approach adopted in this study is based on LES, and, in Section 2.1, we outline the governing equations and the LES methodology. In Section 2.2, we present the subgrid flow models used to describe the small-scale flow physics, in Section 2.3, we present the turbulence chemistry interaction models, and, in Section 2.4, we present the spray combustion models. Finally, in Section 2.5, we describe the numerical methods employed to solve the LES and combustion equations.

2.1. The Gas-Phase Large Eddy Simulation (LES) Methodology

Combustion LES can be divided into two main branches: flamelet LES [13] and finite rate chemistry LES [14]. Independently of branch, the governing equations are the low-pass filtered conservation equations for mass, momentum, and energy, including source terms for the dispersed (droplet) phase. The low-pass filtering is used to separate the resolved flow (denoted by tildes and overbars, depending on the use of density weighted filtering) from the unresolved (subgrid scale) flow. The filtering implies that only the physics of scales larger than the filter width, Δ, are resolved, taking boundary conditions into consideration, while the physics of all scales smaller than Δ are included by their effects on the large scales through subgrid models. For a linear viscous mixture with Fourier heat conduction and Fickian diffusion, the LES equations are [14]:

$$\begin{cases} \partial_t(\overline{\rho}) + \nabla \cdot (\overline{\rho}\widetilde{v}) = \overline{\dot{\rho}_s} \\ \partial_t(\overline{\rho}\widetilde{Y}_i) + \nabla \cdot (\overline{\rho}\widetilde{v}\widetilde{Y}_i) = \nabla \cdot (\overline{\boldsymbol{j}}_i - \boldsymbol{b}_i) + \overline{\dot{w}_i} + \overline{\dot{\rho}_{s,i}} \\ \partial_t(\overline{\rho}\widetilde{v}) + \nabla \cdot (\overline{\rho}\widetilde{v}\otimes\widetilde{v}) = -\nabla\overline{p} + \nabla \cdot (\overline{\boldsymbol{S}} - \boldsymbol{B}) + \overline{\dot{m}_s} \\ \partial_t(\overline{\rho}\widetilde{H}) + \nabla \cdot (\overline{\rho}\widetilde{v}\widetilde{H}) = \partial_t\overline{p} + \nabla \cdot (\overline{\boldsymbol{S}}\widetilde{v} + \overline{\boldsymbol{h}} + \Sigma_{i=1}^{N}(h_{i,f}^{\theta}\overline{\boldsymbol{j}}_i) - \boldsymbol{b}_H) + \Sigma_{i=1}^{N}(\overline{\dot{w}_i}h_{i,f}^{\theta}) + \overline{\dot{q}_s} \end{cases} \quad (1)$$

in which ρ is the density, Y_i the species mass fractions, v the velocity, and $H = h_s + \frac{1}{2}v^2$ the total enthalpy, in which $h_s = \sum_{i=1}^{N}(Y_i \int_{T_0}^{T} C_{p,i}dT)$ is the sensible enthalpy, $C_{p,i}$ the species heat capacity at constant pressure, and T the temperature. The right-hand-side terms include the species mass flux vectors, $\boldsymbol{j}_i \approx D_i\nabla Y_i$, viscous stress tensor, $\boldsymbol{S} \approx 2\mu\boldsymbol{D}_D$, pressure gradient, ∇p, and heat flux vector, $\boldsymbol{h} \approx \kappa\nabla T$, in which D_i is the species diffusivities, μ the viscosity, $p = \rho RT$ the pressure, κ the thermal diffusivity, and R the gas constant. The combustion chemistry enters (1) through the species formation rates, $\dot{w}_i = P_{ij}\dot{w}_j$, and the chemical heat release, $\sum_{i=1}^{N}(\dot{w}_i h_{i,f}^{\theta})$, where $\dot{w}_j$ is the reaction rates, P_{ij} the stoichiometric matrix, and $h_{i,f}^{\theta}$ the formation enthalpies. The dispersed phase is included in (1) through the source terms $\dot{\rho}_s$, $\dot{\rho}_{s,i}$, $\dot{m}_s$, and $\dot{q}_s$, computed by summing the contribution from the DDM [15] used to describe the dispersed phase. Finally, the unresolved transport terms enter (1) through the subgrid species flux vectors, $\boldsymbol{b}_i = \overline{\rho}(\widetilde{vY_i} - \widetilde{v}\widetilde{Y_i})$, stress tensor, $\boldsymbol{B} = \overline{\rho}(\widetilde{v\otimes v} - \widetilde{v}\otimes\widetilde{v})$, and energy flux vector, $\boldsymbol{b}_H = \overline{\rho}(\widetilde{vH} - \widetilde{v}\widetilde{H}) + (\overline{\boldsymbol{S}\widetilde{v}} - \overline{\boldsymbol{S}v})$. Here, D_i and κ are obtained from μ using species Schmidt, Sc_i, and Prandtl, Pr, numbers, following [16]. Equation (1) forms a set of N+5 equations, where N is the number of species but, due to the constraint $\sum_i Y_i = 1$, one species (here Y_{N2}) is discarded.

2.2. LES Subgrid Flow Modeling

The subgrid stress tensor and flux vectors, $\boldsymbol{B}$, $\boldsymbol{b}_H$, and $\boldsymbol{b}_i$, in (1) can be closed using many different models. Sagaut [17] provides a comprehensive review of subgrid models for nonreactive and incompressible flows. Most often, these models are extended to compressible and reactive flows using dimensional arguments. The most prevalent subgrid model is the Smagorinsky (SMG) model [18] and its dynamic extension (DSMG) of Germano et al. [19], which are based on Boussinesq's hypothesis $\boldsymbol{B} = -2\mu_k\widetilde{\boldsymbol{D}}_D + \frac{2}{3}\overline{\rho}k\boldsymbol{I}$, where μ_k is the subgrid viscosity and k the subgrid kinetic energy. Here, $\boldsymbol{b}_H$ and $\boldsymbol{b}_i$ are modeled using the same approach, so that $\boldsymbol{b}_H = (\mu_k/\mathrm{Pr}_t)\nabla\widetilde{H}$ and $\boldsymbol{b}_i = (\mu_k/\mathrm{Sc}_t)\nabla\widetilde{Y}_i$, in which $\mathrm{Pr}_t \approx 0.7$ and $\mathrm{Sc}_t \approx 0.85$ are the turbulent Prandtl and Schmidt numbers, respectively. Alternatively, the one-equation eddy viscosity model (OEEVM) [20] or its dynamic extension, the localized dynamic K-equation model (LDKM) [21], can be used. Here, k is obtained by solving $\partial_t(\overline{\rho}k) + \nabla \cdot (\overline{\rho}k\widetilde{v}) = -\boldsymbol{B} \cdot \widetilde{\boldsymbol{D}} + \nabla \cdot (\mu_k\nabla k) - c_\varepsilon\overline{\rho}k^{3/2}/\Delta$, in which c_k and c_ε are model coefficients, and $\mu_k = c_k\overline{\rho}\Delta\sqrt{k}$. In the OEEVM, c_k and c_ε are obtained from an assumed inertial subrange $\mathrm{k}^{-5/3}$ spectra, whereas, in the LDKM, these coefficients are obtained dynamically using scale similarity [22].

2.3. LES Combustion Modeling

The filtered species formation rates in the species transport equations, $\overline{\dot{w}_i}$, require separate treatment in order to describe the effect of the combustion chemistry on the flow and how the turbulent mixing affects the chemistry. The main reason for this is the inherent nonlinearities in temperature and species mass fractions in the reaction rates, the wide range of scales involved, and the large number of terms that arise due to the reaction mechanism. Several methods to model the filtered species formation rates exist and they can generally be divided into the following classes:

Flamelet models assume that the flame is thin compared to the length scales of the flow and that this region behaves like an interface between fuel and oxidizer (in non-premixed combustion) [23,24] or between reactants and products (in premixed combustion) [25,26]. If scale separation can be assumed, flow and chemistry can be decoupled so that the species transport equations (1_2) may be replaced by transport equations for a mixture fraction, $\widetilde{z}$,

and a reaction co-ordinate or progress variable, $\widetilde{c}$. The chemistry can then be separately computed and tabulated, resulting in a flamelet library parameterized by $\widetilde{z}$ and $\widetilde{c}$ and, if needed, also by other variables, so that $Y_i^{lib} = Y_i^{lib}(z, c)$. The filtered mass fractions, $\widetilde{Y}_i$, can then be computed from $\widetilde{z}$, $\widetilde{c}$, and Y_i^{lib}, using a probability density function (PDF), $\mathcal{P}$, so that $\widetilde{Y}_i = \int_0^1 \int_0^1 \mathcal{P}(z, \widetilde{z}, c, \widetilde{c}) Y_i^{\text{lib}}(z, c) dz dc$. A presumed PDF is often used in which a Beta function is used for z and a clipped Gaussian for c. This requires additional transport equations for the variances of z and c. The source term of $\widetilde{c}$, i.e., $\overline{\dot{w}}_c$, also needs to be modeled [27], e.g., using models based on the flame surface density, Σ, and the laminar flame speed, s_u [28,29], or using tabulated values [30]. Flame surface density (FSD)-based flamelet models are efficient but the source term of $\widetilde{c}$ requires additional modeling [28–31]. Here, we use the Weller et al. model [28], by which Σ is modeled as $\Sigma = \Xi |\nabla \widetilde{c}|$, where Ξ is the flame wrinkling, which, in turn, is modeled by the expression $\Xi = 1 + 2\widetilde{c}(\Theta - 1)$, in which $\Theta = 1 + 0.62(v'\ell_K/v)\sqrt{v'/s_u}$, following [28].

Finite-rate chemistry models are based on the species transport equations (1_2) using closure models for the filtered species formation rates, $\overline{\dot{w}}_i$, explicitly considering the underlying chemical reaction mechanism and its reaction rates. An array of LES finite-rate chemistry models of varying complexity and basic assumptions are available, including the thickened flame model (TFM) [32], the eddy dissipation concept (EDC) [33], the fractal model (FM) [34], the partially stirred reactor (PaSR) model [35], the Eulerian stochastic fields (ESF) model [36], and linear eddy model (LEM) [37]. Based on previous investigations, e.g., [38,39], we, here, use the EDC and PaSR models as representatives of this class of models and, in what follows, we provide further technical specifications of these two finite-rate chemistry LES models.

The EDC model was developed for RANS by Magnussen [40] from the works of Batchelor and Townsend [41], and Chomiak [42] and later modified for LES by Fureby [33]. This modeling reflects the observations that turbulent structures are not uniformly distributed but concentrated in localized regions and that the combustion reactions occur primarily within these fine structures. To model this, the fine structure volume fraction, γ^*, is introduced, resulting in $\widetilde{\psi} = \gamma^* \psi^* + (1 - \gamma^*)\psi^0$ for all variables ψ, where * and ^{0} denote fine structures and surroundings, respectively. This further implies that $\overline{\dot{w}}_i = \gamma^* \dot{w}_i^* + (1 - \gamma_i^*)\dot{w}_i^0$, which may be approximated as $\overline{\dot{w}}_i \approx \gamma^* \dot{w}_i(\overline{\rho}, \widetilde{Y}_k, \widetilde{T})$. A model of the turbulent cascade process was developed in [40] to provide a reliable estimate for the fine structure volume fraction, $\gamma^* \approx 1.02(\nu/\Delta k^{1/2})^{3/4}$.

The PaSR model [35] is based on the same assumptions and approximations as the EDC model, expressing that chemistry occurs in fine structures embedded in an eddy-rich environment, so that $\widetilde{\psi} = \gamma^* \psi^* + (1 - \gamma^*)\psi^0$ for all variables ψ. In the PaSR model, chemical reactions and mixing are treated separately, having different time scales, τ_c and τ_m, respectively. By assuming sequential reaction and mixing steps (in state space), the filtered (or averaged) reaction rates can be shown to become $\overline{\dot{w}}_i \approx \gamma^* \dot{w}_i(\overline{\rho}, \widetilde{Y}_k, \widetilde{T})$, where $\gamma^* = \tau_c/(\tau_m + \tau_c)$. Here, τ_c is modeled as $\tau_c \approx \delta_u/s_u$, in which δ_u is the laminar flame thickness and s_u the laminar flame speed. Similarly, τ_m is modeled as $\tau_m = \ell_D/v_K = \sqrt{\tau_K \tau_\Delta}$, where ℓ_D is the dissipation length scale, v_K the Kolmogorov velocity scale, $\tau_\Delta = \Delta/v'$ the shear time scale, representative of turbulent dissipation, and τ_K the Kolmogorov time scale, representative of mixing at the smallest scales.

2.4. Spray Combustion Models

The discrete droplet model (DDM) is used to represent the spray. Following Dukowicz [43], groups of droplets, all having identical size, location, velocity, and temperature, are represented as computational parcels, tracked using a Lagrangian formulation [15]. The number of particles per group depends on the diameter/volume of the particle in order to avoid unrealistic averaging [44] of the intrinsic droplet properties.

Atomization involves primary breakup of a liquid core into ligaments or large droplets [45], followed by secondary breakup into smaller droplets with negligible effects of collisions [46].

In the vicinity of an injector, both dense and dilute regimes coexist but, downstream, the dilute regime dominates. Here, only the secondary breakup of the injected droplets is considered using the blob-injection method, [47], in which the liquid stream is modeled as a continuous stream of large droplets, blobs, with a characteristic size of the injector diameter. The number of blobs injected is a function of liquid mass flow rate. The injected droplets evolve downstream and undergo secondary breakup, producing new droplets, which are then tracked as parcels. Here, we use the Reitz–Diwakar breakup model [48] that takes into consideration bag and stripping breakup, believed to be the main aerodynamic breakup mechanisms in gas turbines.

Under the assumption that the droplet density is much greater than that of the gas, droplet–droplet interactions are negligible, and the Lagrangian equations of motion for the droplet can be compactly expressed as:

$$\begin{cases} d_t \boldsymbol{x}_p = \boldsymbol{u}_p \\ d_t m_p = -\dot{m}_p \\ d_t \boldsymbol{u}_p = f(\widetilde{\boldsymbol{v}} - \boldsymbol{u}_p)/\tau_v + \boldsymbol{g} \\ m_p c_{p,l} d_t T_p = h_p \pi d_p^2 (\widetilde{T} - T_g) - \dot{m}_p \mathcal{L}_v \end{cases} \tag{2}$$

where $\boldsymbol{x}_p$ is the parcel position, $\boldsymbol{u}_p$ the parcel velocity, $m_p = \frac{4}{3}\rho_p \pi r_p^3$ the parcel mass, with ρ_p the parcel density and r_p the parcel radius, $\dot{m}_p$ the net mass transfer rate, $f = \frac{1}{24} C_D \mathrm{Re}_d$ the drag factor (ratio of the drag coefficient to the Stokes drag), $\tau_v = 4\rho_p r_p^2/18\mu$ the particle velocity response time, $\boldsymbol{g}$ the gravity, $c_{p,l}$ the liquid heat capacity, h_p the heat transfer coefficient, and $\mathcal{L}_v$ the latent heat of vaporization. The drag coefficient C_D is computed following Crowe et al. [49], in which $\mathrm{Re}_d = 2\rho r_d \left|(\widetilde{\boldsymbol{v}} - \boldsymbol{u}_p)\right|/\mu$ is the parcel Re number. The net mass transfer (vaporization) rate is modeled as:

$$\dot{m}_p = \left(1 + \frac{0.278 Re_d^{1/2} Sc^{1/3}}{\left(1 + 1.232/(Re_d Sc^{4/3})\right)^{1/2}}\right) \dot{m}_{p,Re_d=0} \tag{3}$$

where $\mathrm{Re}_d = 0$ is the Re number for particle at rest. Under quiescent conditions, the mass transfer rate reduces to $\dot{m}_{p,\mathrm{Re}_d=0} = 4\pi\rho_s D_s r_p \ln(1 + B_M)$, in which ρ_s and D_s are the density and diffusivity at the parcel surface and B_M the Spalding mass transfer number. The heat transfer coefficient is approximated by the Ranz–Marshall model [50], in which $h_p = \kappa \mathrm{Nu}_p/2r_p$, where the particle Nusselt number is $\mathrm{Nu}_p \approx 2 + 0.6\mathrm{Re}_p^{1/2}\mathrm{Pr}^{1/3}$.

The Eulerian–Lagrangian coupling is through the interphase exchange terms: if n_p number of droplets are present per parcel/group, then the volume-averaged source terms for all the droplet parcel/group trajectories that cross a computational cell (of volume dV) are computed by summing the contribution from every parcel or group as:

$$\begin{cases} \overline{\dot{\rho}_s} = \frac{1}{dV}\sum_m n_p[\dot{m}_p] \\ \overline{\dot{\rho}_{s,i}} = \frac{1}{dV}\sum_m n_p[\dot{m}_p] \\ \overline{\dot{m}_s} = \frac{1}{dV}\sum_m n_p[\dot{m}_p \boldsymbol{u}_p - m_p d_t \boldsymbol{u}_p] \\ \overline{\dot{q}_s} = \frac{1}{dV}\sum_m n_p[\dot{m}_p h_{v,s} - h_p 4\pi r_p^2 (T - T_p) - \boldsymbol{u}_p m_p d_t \boldsymbol{u}_p + \frac{1}{2} m_p \boldsymbol{u}_p^2] \end{cases} \tag{4}$$

where the summation index m is overall the droplet parcels/groups crossing a computational cell (of volume dV). Moreover, note that the species source term, $\overline{\dot{\rho}_{s,i}}$, for all species, i, is *zero*, except for the species that is present in liquid form and evaporating.

2.5. Numerical Methods

The LES equations are solved using a finite volume-based code developed from the OpenFOAM C++ library [51], which, in turn, is based on an unstructured collocated finite volume method using Gauss's theorem. The time integration is performed with a semi-implicit second-order accurate two-point backward differencing scheme [52] for premixed

flames and the single-point implicit Euler scheme for spray flames. The convective fluxes are reconstructed using multi-dimensional cell limited linear interpolation, whereas diffusive fluxes are reconstructed using a combination of central difference approximations and gradient face interpolation. Here, a compressible version of the pressure implicit with splitting of operators (PISO) method [53] is used to discretize the pressure–velocity–density coupling, using the thermal equation of state. The combustion chemistry is integrated separately, using a Strang-type operator-splitting algorithm [54] and a Rosenbrock time-integration scheme [55,56] for the resultant system of differential equations. The algorithm is second-order accurate, and the equations are solved sequentially with a Courant number limitation of approximately 0.5.

3. Kerosene-Grade Fossil and Non-Fossil Jet Fuels

Jet fuel is a multi-component fuel with a carbon chain length of C8–C16 [57], initially developed from lamp oil. The specifications of jet fuel have been developed and changed in order to meet standards of engine compatibility, safety, and security of supply [58]. The most used jet fuels are kerosene-grade fuels derived from petroleum, such as Jet A, JP5, and JP8 [59]. Between 75% and 90% of the jet fuel is made up of normal, branched, and iso-paraffins, with cycloparaffins and aromatics also present. A higher hydrogen-to-carbon weight ratio, H/C, for normal, branched, and iso-paraffins gives a higher heat-to-weight ratio and a cleaner combustion. The cyclo-paraffins reduce the H/C ratio, the heat release per unit weight and the freeze point. Aromatics should be present at between 8 vol % and 25 vol% for material interactions, lubricity, and swelling effects.

Fossil and non-fossil jet fuels typically have different compositions, which is most likely also reflected in their thermodynamic, spray, and combustion properties. Based on requirements defined in the US CRATCAF program [60], the US NJFCP program [61] has developed a suite of conventional and alternative jet fuels to characterize the combustion sensitivity to fuel specifications. Following [62], these fuels can be grouped into Category A fuels composed of fossil kerosene-grade jet fuels spanning the range of properties typically encountered; Category B fuels, which are alternative jet fuels with unacceptable combustion properties (not further considered); and Category C fuels, which are alternative jet fuels designed to explore the edges of the jet fuel composition–property space. The Category A fuels consist of three specific jet fuels: A1 being a fuel with low flash/viscosity/aromatics corresponding to JP8, A2 being a fuel with average/nominal properties corresponding to Jet A, Figure 1a, and A3 being a fuel with high flash/viscosity/aromatics corresponding to JP5, Figure 1b. The derived cetane numbers (inversely proportional to the ignition delay time) of A1, A2, and A3 are 38, 48, and 43, respectively, which is normal for a jet fuel. As a reference, we can mention that the cetane number of n-dodecane ($C_{12}H_{26}$) is 76. The Category C fuels consist of six different hydrocarbon blends spanning a range in cetane number, aromatics, viscosity, and flash. As an example, we, here, consider C1. C1, Figure 1c, was designed to be the lowest cetane number jet fuel available, which turned out to be the Gevo ATJ fuel, consisting primarily of C12 and C16 iso-paraffins, with a cetane number of 17.

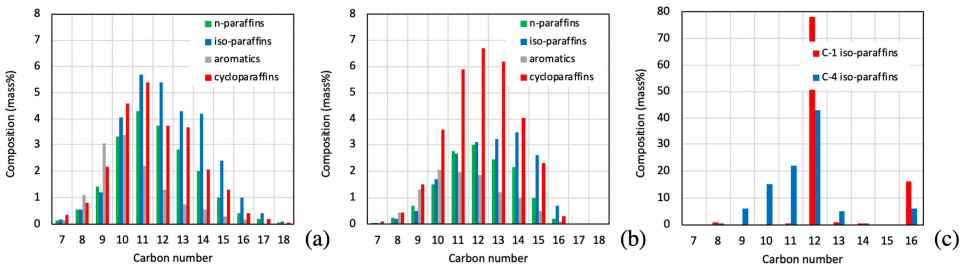

Figure 1. Hydrocarbon distribution plots of selected Category A and Category C jet fuels: (**a**) A2 or Jet A, (**b**) A3 or JP5, and (**c**) C1 and C4. Data extracted from [62].

The chemical composition influences the thermophysical properties and the combustion behavior (to be discussed in Section 4). Table 1 summarizes the central thermophysical properties of the fuels used in the present study (n-dodecane, Jet A, and C1), as well as the category A fuel A3 (representing JP5) and the category C fuel C4.

Table 1. Main thermophysical properties of selected Category A and C fuels [62].

Property	*n-Dodecane*	*Jet A, A2 (POSF 10325)*	*JP5, A3 (POSF 10289)*	*C1 (POSF 11498)*	*C4 (POSF 12344)*
Density (kg/m^3)	749	803	827	760	760
Viscosity @ 20 °C (cSt)	1.34	4.5	6.5	4.9	3.9
Surface tension (mN/m)	22.1	25.8	26.1	22.4	—
Aromatics (vol. %)	0	17.0	18.0	1.0	2.3
Heat of combustion (MJ/kg)	46.5	43.3	43.1	44.2	43.8
H content (wt. %)	15.2	14.0	13.7	15.3	15.5
Cetane number	74.7	48.3	39.2	17.1	28

4. Combustion Chemistry

The fuels of interest in the simulations are n-dodecane, Jet A, and C1. In order to model the combustion of these fuels, we adopted the SK54 reaction mechanism developed by Yao et al. [63] for n-dodecane, while HyChem reaction mechanisms developed by Wang et al. [64] were used to model Jet A and C1. The development of SK54 was based on the assumption that the kinetics of fuel pyrolysis at high temperatures, described by the sub-mechanism of C_5-C_{12}, can be isolated from the H_2 and C_1-C_4 reactions and first simplified by cutting off unimportant species and reactions, and then merged into a simplified $H_2/CO/C_1$-C_4 base mechanism [63]. The approach for the development of the HyChem reaction mechanisms is that the fuel pyrolysis and the pyrolysis products' oxidation are expressed in two different but interconnected sub-models. Pyrolysis offers reactants for the oxidation process, while the oxidation provides heat and radicals to facilitate the endothermic fuel pyrolysis. The first process is modeled by several experimentally constrained, lumped reaction steps and the second is based on a comprehensive foundational chemistry model. Although several versions of the HyChem mechanisms are available, we have used the skeletal versions with the negative temperature coefficient (NTC) effect enabled when possible. The n-dodecane and Jet A mechanisms support the NTC effect, while the C1 mechanism does not. The n-dodecane SK54 mechanism has 54 species and 269 reactions. The HyChem mechanism for Jet A has 48 species and 254 reactions, whereas the HyChem mechanism for C1 has 42 species and 286 reactions, making these reaction mechanisms moderately complex.

Figure 2 compares predictions of the laminar flame speed, s_u, extinction strain rate, σ_{ext}, and ignition delay time, τ_{ign}, between dodecane, Jet A, and C1 with experimental data from [65–71]. Numerical simulations are made using Chemkin [72] under the conditions reported in [65–71]. Laminar flames at 1 atm and equivalence ratios ranging from 0.6 to 1.6 are studied to extract s_u at $T = 403$ K. The corresponding experimental results were gathered at $T = 403$ and 400 K. The extinction strain rate computation is conducted using a counterflow diffusion flame at atmospheric pressure conditions and temperatures equal to 473 K and 300 K for the fuel and the oxidizer, respectively. The ignition delay time is computed for 10.0 atm at stochiometric conditions, with experimental results gathered for stoichiometric mixtures between $p = 12.0$ atm and $p = 14.8$ atm.

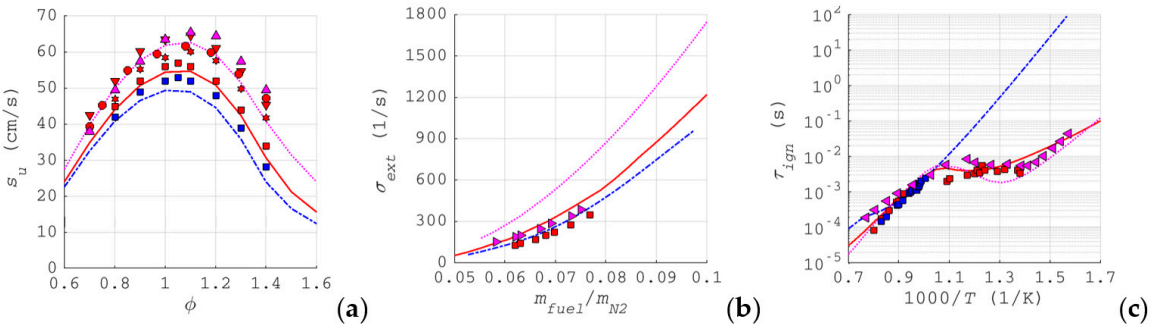

Figure 2. (**a**) Laminar flame speed (s_u), (**b**) extinction strain rate (σ_{ext}), and (**c**) ignition delay time (τ_{ign}) for n-dodecane ( ), Jet A ( ), and C1 ( ). Lines denote the numerical predictions, while symbols the experimental data from Kumar et al., [65] (▲), Xu et al. [66] (■, ■), Dooley et al. [67] (▼), Hui et al. [68] (✸), Kumar et al. [69] (●), Liu et al. [70] (▸), and Mao et al. [71] (◂).

The laminar flame speed results show how the SK54 reaction mechanism agrees well with the experimental results from Kumar et al. [65] for lean mixtures. However, above the stoichiometric conditions, the numerical predictions deviate from the experiments, with the resulting offset increasing with the equivalence ratio, ϕ, from 2.85% at $\phi = 1$ to 21.34% at $\phi = 1.4$. This underprediction may be due to the simplified sub-mechanism for C_5–C_{12} species, the presence of which is relevant at rich conditions. The laminar flame speed, s_u, trends show how the HyChem reaction mechanism for Jet A agrees well with the experimental results from Xu et al. [66], in which the HyChem mechanisms were validated during their development. On the other hand, the HyChem mechanism for C1 slightly underpredicts the flame speeds, especially at lean conditions, showing a maximum error of 18% at $\phi = 0.7$. Some discrepancies between experiment and numerical simulations become evident when comparing the Jet A HyChem results for s_u with those from Dooley et al. [67], Hui et al. [68], and Kumar et al. [69].

Despite the differences in lower heating value between n-dodecane, C1, and Jet A, the reaction mechanisms behave similarly at lean and stoichiometric conditions, showing virtually the same flame temperature (not shown). Notable differences are visible when examining σ_{ext} and τ_{ign}. For σ_{ext}, the simulations predict a higher resistance to extinction for n-dodecane and Jet A than C1, overestimating also the σ_{ext} values when compared with experimental results [66–70]. The disagreement for the n-dodecane results is larger than the discrepancies related to Jet A. Not surprisingly, this can be due to the incapability of the skeletal mechanism for n-dodecane to describe a behavior closer to reality for C_5–C_{12} molecules, the presence of which in the fuel mixture tends to reduce the magnitude of σ_{ext}. Regarding the ignition delay time, τ_{ign}, all the investigated fuels behave similarly in the high-temperature regime, showing qualitatively good agreement between numerical simulations and experiments. Some minor underpredictions are visible in the numerical results from n-dodecane when compared with experimental data from Mao et al. [71]. However, it is evident how, at low temperature only, SK54 and the HyChem mechanism for Jet A are able to capture the experimental trends, as only these two mechanisms contain sub-models for low-temperature chemistry, which enable the NTC effect.

5. Results from LES

In this study, we consider three different combustor configurations: a pre-vaporized premixed bluff-body stabilized flame, a generic single-cup spray combustor, and a single-sector model of a helicopter engine. The pre-vaporized premixed bluff-body stabilized flame serves to validate the combustion chemistry modeling and the turbulence chemistry interaction modeling, and to provide information about how Jet A and C1 burns in a turbulent environment. The single-cup spray combustor serves to investigate the influence of turbulent spray combustion and focuses on comparing turbulent spray combustion for Jet A and C1. Finally, the single-sector model helicopter engine is intended to demonstrate

that we can differentiate between fossil (Jet A) and non-fossil fuels (C1) not only with respect to combustion, but also with respect to emissions.

5.1. Air Force Research Laboratory (AFRL) Combustor

The first combustor configuration considered here is the equilateral triangular bluff-body combustor of Air Force Research Laboratory, Wright-Patterson Air Force Base [73], presented in Figure 3. During operation, electrically heated air passes a vitiator dome, a single-stage radial cyclone swirl combustor, and a mixing cone to promote uniform temperature across the critical plate, being the inlet section for the simulations, acoustically isolating the test section from the upstream supply section. Downstream of the critical plate, the hot air passes around the fuel spray bars, each with nine injection orifices, into the flow development section, where boundary layer and turbulence effects are used to produce a fully developed premixed flow at the test section inlet. The test section is of rectilinear shape, with a cross-section of 152.4 $\times$ 127.2 mm^2. The bluff body is a solid $h = 38.1$ mm equilateral triangle, and the test section exit is open to the atmosphere. High-frequency pressure transducers mounted along the streamwise and transverse directions and high-speed OH* chemiluminescence is performed to characterize the flame.

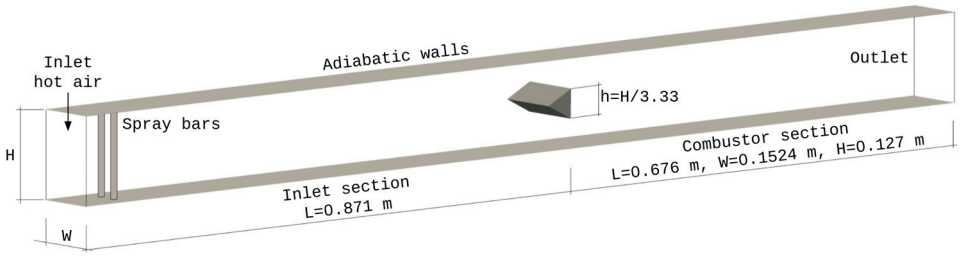

Figure 3. Schematic of the simulation domain used for the AFRL bluff-body combustor.

In the experimental study of Paxton et al. [73], four different jet fuels were tested, including n-dodecane, Jet A (or A2), JP5 (or A3, not considered here), and the test jet fuel C1. These fuels explore a range of different chemical parameters, most notably, the cetane number, which is inversely proportional to τ_{ign} and functions as an indicator of ignition quality. A previous study using propane (C_3H_8) was also carried out in this combustor [74,75], which, in turn, was validated against earlier experimental data [76,77]. Finite rate chemistry LES modeling was performed in [78,79] and compared with the data in [74–77], showing excellent agreement. As part of this comparison, a grid refinement study was also performed with grid sizes ranging from 3.7 to 99.6 million cells. From this grid refinement investigation, it was concluded that the grids used should resolve more than 90% of the total kinetic energy and have a grid size of less than 0.5 mm.

The grids used here are of hexahedral type and simulations have been performed on a coarse grid of 6.8 million cells and a medium grid of 23 million cells, both with grid sizes less than 0.5 mm in the combustion region. For these grids 92% and 96% of the total kinetic energy is resolved, making both grids acceptable for LES. Below, simulation results will be presented for the medium-grid LES simulations only.

To provide an overview of the flow and the flame in the simulations, Figure 4 presents instantaneous images of the axial velocity, $\widetilde{v}_x$, second invariant of the velocity gradient tensor, λ_2, temperature, $\widetilde{T}$, heat release, $\log(Q)$, and mass fractions, $\widetilde{Y}_i$, of i-C_4H_8, CH_2O, HCO, and OH from combustion of C1 using the LDKM and EDC models. The other cases investigated, using dodecane and Jet A, behave similarly but with fuel-associated differences, as will be subsequently discussed. The species were selected from examining reaction-path diagrams from which it appears that i-C4H8 is the main fuel breakdown product; CH_2O and HCO are along one of the major pathways to the production of CO, whereas OH represents the post-flame region dominated by end-products, such as CO_2. Figure 4a show that spanwise, $\widetilde{\omega}_z$, vortex structures are simultaneously shed off the upper and lower corners of the flameholder, whereas longitudinal, $\widetilde{\omega}_{xy}$, vortex structures form in

the regions between neighboring $\widetilde{\omega}_z$ vortex structures, resulting in two initially symmetric vortex braids that gradually widen and lose their symmetry due to vortex–vortex interactions under the influence of exothermicity and baroclinic torque effects. These vortex braids enclose most of the recirculation zone developing behind the flame holder. Note also how $\widetilde{\omega}_z$ and $\widetilde{\omega}_{xy}$ vortices tend to form large vortex structures downstream of the closure of the recirculation region, where the vortex braids have lost most of their symmetry. The formation of the $\widetilde{\omega}_z$ vortex structures are due to Kelvin–Helmholtz instabilities, whereas the downstream larger vortex structures are due to Bénard–von-Karman instabilities. The ratio of burnt-to-unburnt temperatures is $T_b/T_u \approx 3.3$, which, according to [80], favors early transition from symmetric to asymmetric vortex shedding. The vortex braids are responsible for mixing of premixed fuel and air with hot combustion products recirculated by the wake, resulting in heating of the vortex braids from within, hence creating a stable flame-anchoring mechanism. The $\widetilde{T}$ distribution of Figure 4b, as well as the $\log(Q)$ distribution of Figure 4c reflect the initial symmetric shedding, followed further downstream by asymmetric vortex shedding. Heat release occurs primarily in a reasonably well-defined flame front, wrinkled and furrowed by the $\widetilde{\omega}_z$ and $\widetilde{\omega}_{xy}$ structures and the turbulence. In Figure 4d, the species distributions are presented. From this, it follows that combustion occurs predominantly in layers, with the outer layer(s) dominated by the breakdown of the fuel to intermediates, such as i-C_4H_8, followed, in turn, by further conversion into CH_2O, HCO, and OH, the latter correlating with $\log(Q)$. The observed behavior is fully in line with that observed also for propane, e.g., [79].

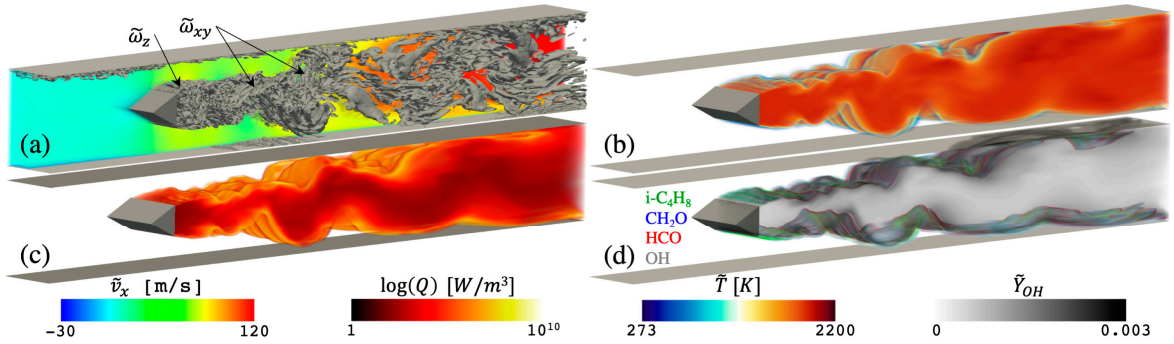

Figure 4. Instantaneous perspective views from the side of the reacting flow in the AFRL equilateral triangular bluff-body combustor in terms of (**a**) volume renderings of the axial velocity, $\widetilde{v}_x$, and an iso-surface of the second invariant of the velocity gradient tensor, λ_2, (**b**) temperature, $\widetilde{T}$, (**c**) heat release, $\log(Q)$, and (**d**) mass fractions, $\widetilde{Y}_i$, of i-C_4H_8, CH_2O, HCO, and OH for C1.

As the flame is thin, wrinkled and furrowed by vorticity and turbulence, the flamelet model [25–31] appears attractive, since the finite rate chemistry models [14,32–37] are expensive for comprehensive reaction mechanisms. To examine the differences between the flamelet and finite rate chemistry models, Figure 5 compares line-of-sight OH* chemiluminescence images from the n-dodecane experiments, with similar images from flamelet LES, using the FSD model of Weller et al. [28] and the LES-LDKM-EDC model for n-dodecane, Jet A, and C1 at $\phi = 0.66$. For both models, the OH* chemiluminescence is derived following Ehn [81]. The FSD model predictions appear to be dominated by almost two-dimensional undulations with weak superimposed spanwise waves associated with the longitudinal vortices $\widetilde{\omega}_{xy}$. In contrast, the LES-LDKM-EDC model predictions show strong three-dimensional furrows and crinkles. These differences appear to be inherent to the flamelet and finite rate chemistry models, with the turbulence chemistry interactions allowed to influence the flame structures more locally for the finite rate chemistry models. Compared with the experimental OH* chemiluminescence images, it seems as if the finite rate chemistry models represent the flame in a more realistic manner. The computational expense of FRC-LES, with $O(300)$ reactions and $O(50)$ species, compared to flamelet LES,

is about an order of magnitude higher. Conversely, we, here, use the finite rate chemistry models for the remaining spray combustion studies.

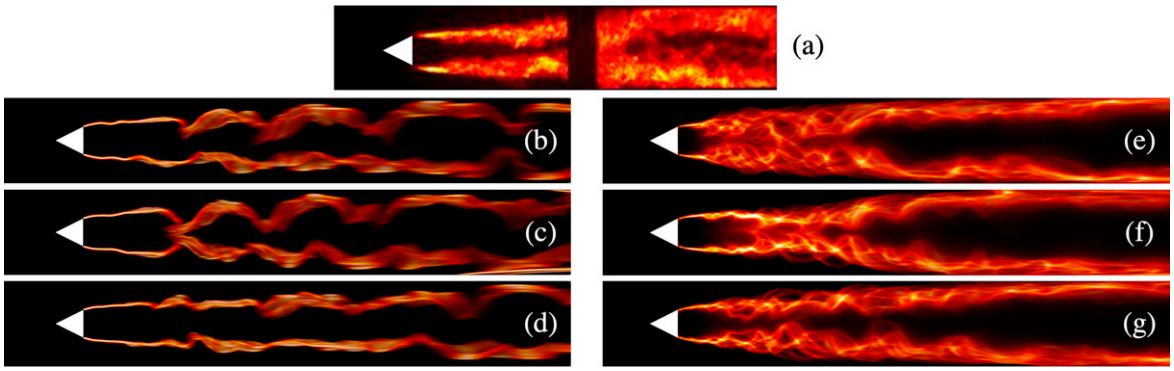

Figure 5. OH* chemiluminescence images from (**a**) experiments with n-dodecane, and from flamelet LES, using the FSD model of Weller et al. [28] of (**b**) n-dodecane, (**c**) Jet A, and (**d**) C1, and from LES-LDKM-EDC model of (**e**) n-dodecane, (**f**) Jet A, and (**g**) C1 at $\phi = 0.66$.

Figure 6 shows comparisons of the time-averaged axial velocity, $\langle \widetilde{v}_x \rangle$, and axial velocity fluctuation, v_x^{rms}, profiles along the vertical direction, y/h, at $x/h = 0.375$, 0.95, 1.53, 3.75, and 9.40, normalized with the inflow velocity, v_0, from the LES-LDKM-EDC simulations of n-dodecane, Jet A, and C1 at an equivalence ratio of $\phi = 0.66$. Regarding $\langle \widetilde{v}_x \rangle$, we find that, at $x/h = 0.375$, where x refers to the axial co-ordinate, all fuels show U-shaped $\langle \widetilde{v}_x \rangle$ profiles. At $x/h = 0.95$, n-dodecane and C1 show V-shaped profiles, whereas Jet A still shows a U-shaped $\langle \widetilde{v}_x \rangle$ profile. At the end of the recirculation zone, at $x/h = 1.53$, all fuels behave similarly, showing V-shaped $\langle \widetilde{v}_x \rangle$ profiles. In the recovery region, represented by the profile at $x/h = 3.75$, Jet A shows the slowest recovery. In the fully developed turbulent combustion region, represented by the profile at $x/h = 9.40$, all fuels tend to predict almost flat $\langle \widetilde{v}_x \rangle$ profiles. Regarding v_x^{rms}, we find that the v_x^{rms} profile shapes are similar, with the highest fluctuation levels initially occurring in the shear layers, then transitioning towards the center of the duct at the end of the recirculation zone, and, finally, to spread out across the duct in the fully developed turbulent combustion region, where v_x^{rms} is highest for n-dodecane followed by C1 and Jet A.

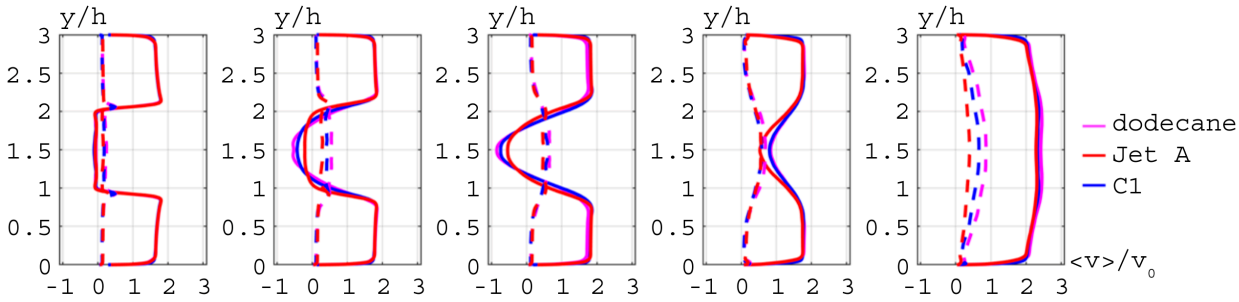

Figure 6. Comparison of time-averaged axial velocity, $\langle \widetilde{v}_x \rangle$, and axial rms velocity fluctuations, v_x^{rms}, at $x/h = 0.375$, 0.95, 1.53, 3.75, and 9.40, from left to right, between the LES-LDKM-EDC simulations of n-dodecane, Jet A, and C1 at $\phi = 0.66$.

Figure 7 presents comparisons of the time-averaged temperature, $\langle \widetilde{T} \rangle$, and temperature fluctuation, T^{rms}, profiles at $x/h = 0.375$, 0.95, 1.53, 3.75, and 9.40, normalized by the adiabatic flame temperature, T_{ad}, from the LES-LDKM-EDC simulations of n-dodecane, Jet A, and C1 at $\phi = 0.66$. Regarding $\langle \widetilde{T} \rangle$, we find that, at $x/h = 0.375$, all fuels give virtually identical $\langle \widetilde{T} \rangle$ profiles. At the end of the recirculation zone, represented by $x/h = 1.53$, the $\langle \widetilde{T} \rangle$ profiles are still similar, with n-dodecane showing a slightly lower peak temperature. In the recovery region, here represented by the profile at $x/h = 3.75$, all $\langle \widetilde{T} \rangle$ profiles are

wider and smoother, with that of n-dodecane being the widest and that of Jet A being the narrowest. In the fully developed turbulent combustion region, here represented by the profile at $x/h = 9.40$, the ordering is the same but the differences are now less pronounced. Regarding T^{rms}, we find very similar profiles between the fuels, with n-dodecane showing slightly higher values in the recirculation zone.

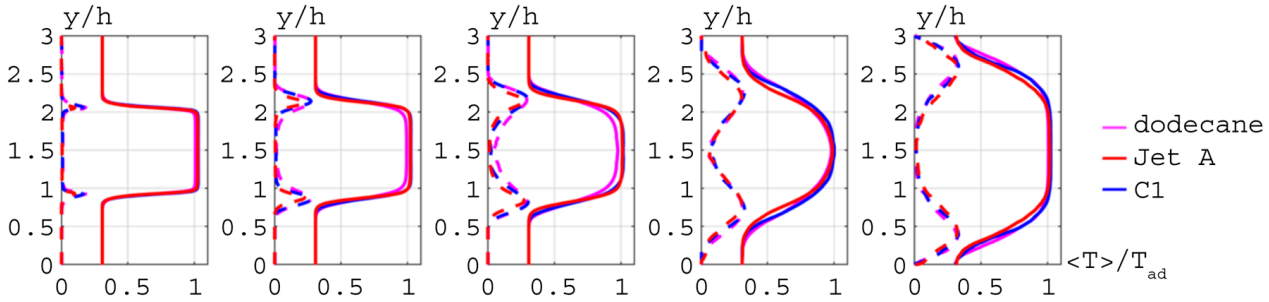

Figure 7. Comparison of time-averaged temperature, $\langle \widetilde{T} \rangle$, and rms temperature fluctuations, T^{rms}, at $x/h = 0.375$, 0.95, 1.53, 3.75, and 9.40, from left to right, between the LES-LDKM-EDC simulations of n-dodecane, Jet A, and C1 at $\phi = 0.66$.

Figure 8 presents comparisons of the time-averaged CO concentrations, $\langle \widetilde{Y}_{CO} \rangle$, profiles at $x/h = 0.375$, 0.95, 1.53, 3.75, and 9.40 from the LES-LDKM-EDC simulations of n-dodecane, Jet A, and C1 at an equivalence ratio of $\phi = 0.66$. The $\langle \widetilde{Y}_{CO} \rangle$ profiles in the recirculation zone, represented by $x/h = 0.375$, 0.95, and 1.53, show some differences with the highest $\langle \widetilde{Y}_{CO} \rangle$ values occurring in the spatially developing shear layers for Jet A, followed by C1 and n-dodecane. In the fully developed turbulent combustion region, represented by $x/h = 9.40$, all profiles are virtually identical. The higher fluctuation levels (in v_x^{rms} and T^{rms}) for dodecane and C1, compared to Jet A, are closely related to the higher pressure fluctuation levels observed also for dodecane and C1, which, in turn, are related to the differences in composition and chemistry of these fuels. This is also partly reflected in the different cetane numbers of these fuels.

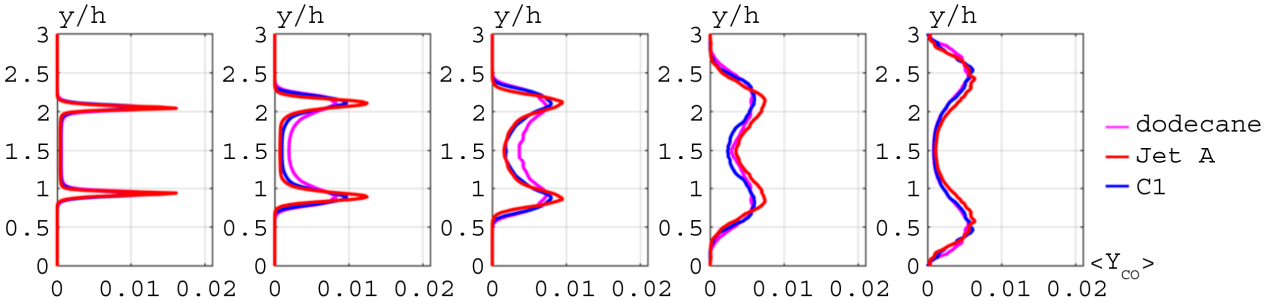

Figure 8. Comparison of time-averaged CO concentrations, $\langle \widetilde{Y}_{CO} \rangle$, at x/h = 0.375, 0.95, 1.53, 3.75, and 9.40, from left to right, between the LES-LDKM-EDC simulations of n-dodecane, Jet A, and C1 at an equivalence ratio of $\phi = 0.66$.

5.2. DLR Single-Cup Swirl Combustor

The second simulation case presented in this paper is based on a test rig studied at DLR Institute of Propulsion Technology [82,83]. Numerical studies of this case have previously been carried out with LES [84,85], SAS [85,86], and RANS [86]. We have also previously reported on it in [87], where the impact of reaction mechanism complexity was gauged. With a length of 0.264 m and a square cross-section of 102 × 102 mm^2, the combustor is designed to be an appropriate representative of a single-sector aeroengine combustor with liquid fuel injection. The geometry of the rig, as it is used in our study, is presented in Figure 9, along with some key results to visualize the flow and combustion.

Air is supplied to a burner equipped with two co-rotating swirlers, which cause the air flow to swirl about the central axis (the z axis). Liquid kerosene is injected along the inner burner wall just upstream of the combustion chamber. At the end of the pre-filmer lip, the liquid film is atomized by the strongly rotating air flow, causing the fuel to enter the combustor as a cone-shaped cloud of dispersed droplets with diameters of less than 30 µm. In the simulations, the fuel is assumed to be atomized already at the point of injection. The swirlers give rise to a flow pattern inside the combustion chamber that consists of a central recirculation zone (CRZ) of reversed flow. The CRZ is enveloped by a main flow cone (MFC) with axial flow (visualized by arrows), and an outer recirculation zone (ORZ) is formed near the corners of the combustor base. The fuel quickly evaporates and ignites in the MFC due to the high temperature in the combustor, and the resulting flame is kept stable near the inner shear layer that forms the highly turbulent boundary between the CRZ and the MFC. Hot combustion products are recirculated towards the spray, continually heating it. A choked converging nozzle is used at the outlet for pressure control. The test rig has been operated with pressures, temperatures, and mass flows that represent both idling and cruise conditions in a typical aeroengine, though, here, we will only consider cruise conditions. Air at 650 K and 10 bar is supplied to the burner at a rate of 140 g/s and to the walls at a rate of 39 g/s (for cooling). Liquid fuel is injected at a rate of 6.8 g/s, resulting in a global equivalence ratio of 0.74 (counting the burner air flow only).

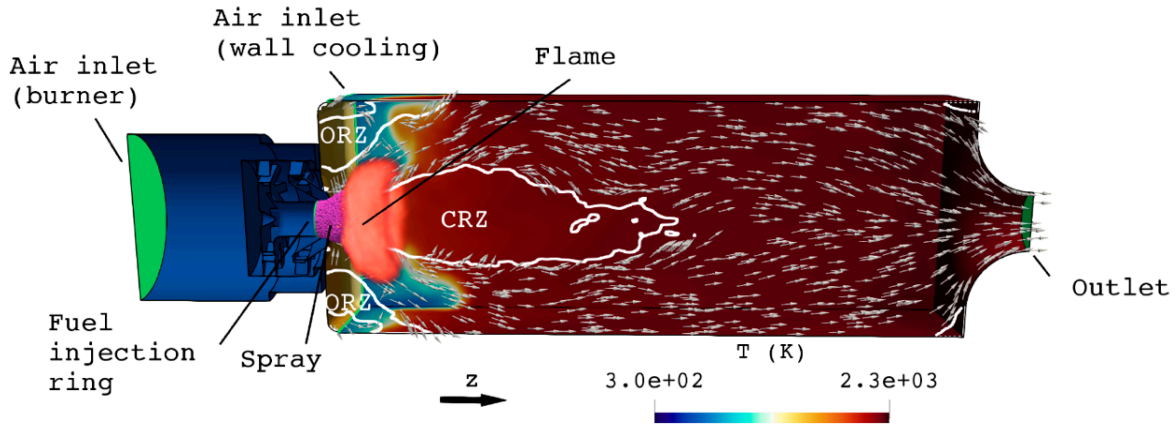

Figure 9. Centrally cut geometry with LES results. Inlets are green, and walls are colored by time-averaged temperature. The spray is colored in magenta, and the time-averaged flame is colored in light red. Arrows indicate mean velocity direction in the central plane inside the main flow cone (MFC). The central (CRZ) and outer (ORZ) recirculation zones are denoted by white contours.

A block-structured hexahedral mesh of 6.0 million cells is used to discretize the LES Equation (1). The cell size is roughly uniform throughout the domain, which means that the near-wall flow behavior has to be accounted for by a wall model based on Spalding's law of the wall [88]. Approximately 85% of the total turbulent kinetic energy belongs to the resolved scales, on average. The mass flux at the air inlets is fixed, and the fuel injection ring is treated as a wall for the Eulerian phase. A wave-transmissive boundary condition is used at the outlet, which allows the pressure to be controlled but avoids unphysical wave reflection. All walls are considered adiabatic. Following (2), Lagrangian particles, representing groups of fuel droplets, are introduced uniformly along the injection ring, with diameters chosen randomly following a Rosin–Rammler probability distribution, as described in [84]. Simulations are initialized from a simple state where the combustion chamber is filled with burnt gas, after which they are run until a statistically steady state is achieved. Temporal averages are constructed over 10 ms. Figure 10 presents the time-averaged flame shapes based on heat release rate (simulations) and deconvoluted OH* chemiluminescence (experiments). The simulated flames for both Jet A and C1 are qualitatively similar to experimental observations. The heat release is spread out along

the inner shear layer in the C1 flame, while it is more concentrated around $r = 30$ mm in both the experiments and the simulated Jet A flame. The closer resemblance of Jet A to the experiments is expected as a conventional jet fuel was used in the experiments.

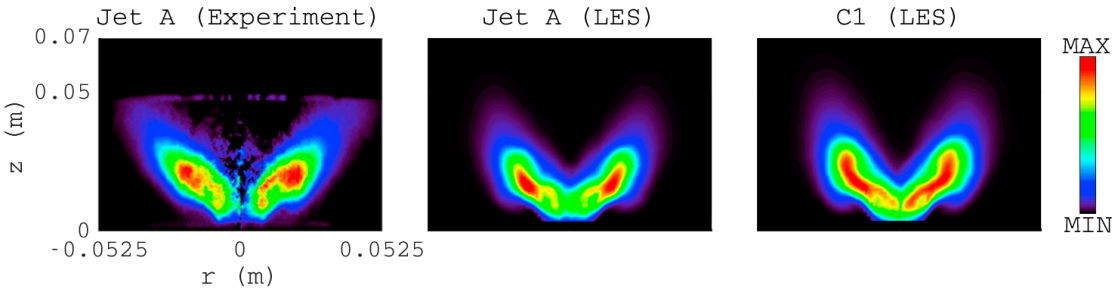

Figure 10. Time-averaged flame shape in the experiments (**far left**) and simulations (**middle** and **right**). Experimental results taken from [83].

Flames are often described as premixed or non-premixed, depending on whether or not the unburnt fuel is mixed with the oxidizer before combustion. Swirl-stabilized spray flames do not fit into either category, as they may have features from both. If the flame is very close to the spray, combustion occurs rapidly after the fuel evaporates and comes into contact with the surrounding air. This is similar to a non-premixed flame. There may also be significant mixing between gaseous fuel and oxidizer before combustion, resulting in a more premixed-like flame. The Takeno Flame Index (TFI) provides a way to quantify how premixed or non-premixed a combustion process is based on the gradients of the gaseous fuel and oxidizer concentrations [89]. If these gradients are parallel, the combustion is considered to be premixed and TFI $= 1$. If they are anti-parallel, the combustion is considered to be non-premixed and TFI $= 0$. Figure 11 shows snapshots of the spray and flame for both simulated fuels. The leftmost panel is included for reference and contains a full three-dimensional rendering, with volume renderings of gaseous fuel (pure green) and heat release (following a color scale). The center and right panels show results in a central slice of the domain. A contour of $Q = \max(Q)/10$, where Q is the heat release rate, reveals a thin turbulent flame front downstream of the spray (magenta). Based on the TFI, non-premixed regions are shown in black and premixed regions in gray. The TFI is virtually uniform (either 0 or 1) within these regions. Regions without any substantial concentration of the fuel species are uncolored. It appears that the heat release is primarily occurring in the premixed mode; the fuel and oxidizer are mixed before combustion, which means that the gradients of their mass fractions are parallel across the flame front. We conclude that the simulated flames behave as premixed flames.

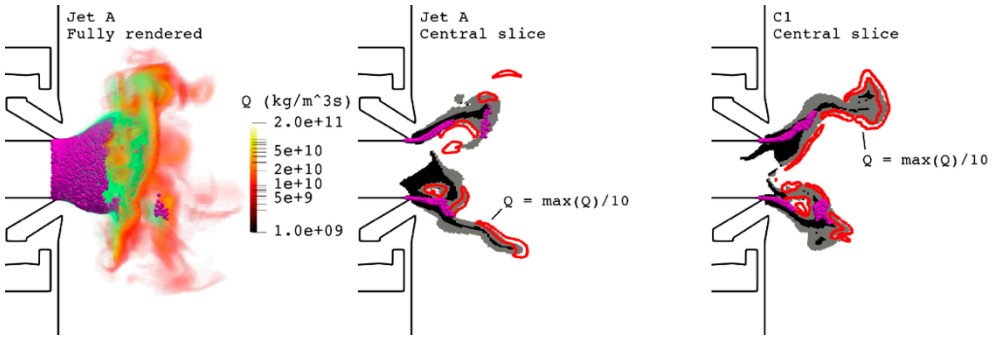

Figure 11. Snapshots of the simulated spray flame with walls included. Magenta: spray. Green: gaseous fuel. **Left** panel: fully rendered spray and flame for Jet A. The volume rendering of heat release (Q) is colored following a logarithmic scale. **Center** (Jet A) and **right** (C1) panels: central slice, with non-premixed regions in black and premixed regions in gray. Red: contour of $Q = \max(Q)/10$.

To better understand the evolution of the fuel spray, the mean radial profiles of the diameter, d_p, and temperature, T_p, of the spray droplets are plotted in Figure 12 at three locations downstream of the burner. Experimental measurements [83] of the Sauter mean diameter (SMD) are included for comparison. At $z = 10$ mm, where z is the axial distance from the burner, the fuel temperature has increased by 200 to 290 K from its injection temperature of 298 K. Recirculated combustion products in the ORZ heat the outermost droplets, giving them a high temperature. The CRZ has the same effect close to the centerline, though this is more obvious at $z = 15$ mm and $z = 20$ mm, where the CRZ has a higher concentration of hot combustion products than at $z = 10$ mm. The saturation temperature at 10 bar is 616 K, forming the upper limit of the droplet temperature. The global temperature minima correspond to small local diameter maxima, which is logical, as low temperature leads to slow evaporation and, hence, relatively large droplets. Intuitively, one would then expect the inner- and outermost droplets to have the smallest diameters, as they are subjected to the most heating. However, this does not appear to be the case for the outermost droplets, which are relatively large, despite being heated by the ORZ. This can be explained by noting that large droplets have higher inertia than small droplets [83], resulting in higher radial velocity in the swirling flow. Therefore, the droplets that reach far from the centerline tend to be large initially. The same phenomenon contributes to the small droplet sizes seen near the centerline.

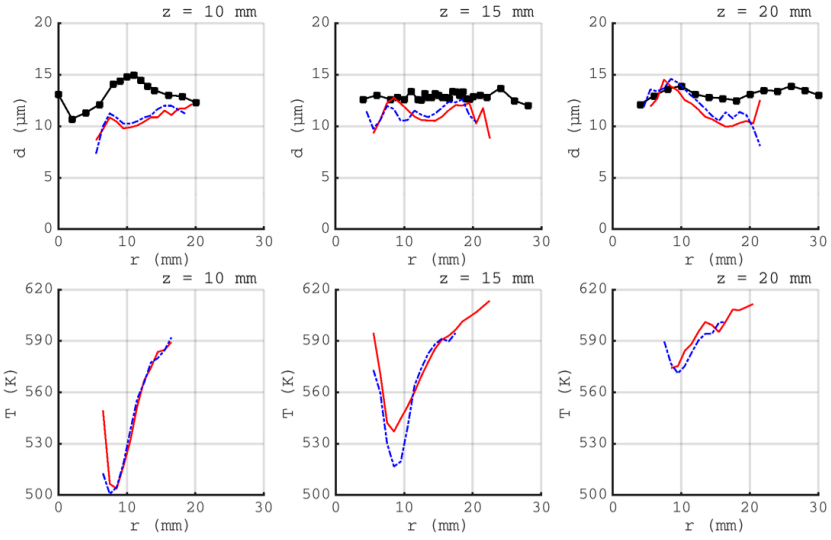

Figure 12. Radial distributions of time-averaged diameter (**top**) and temperature (**bottom**) at three different axial locations. Experimental data from [83]. Legend: experiment (—), Jet A (—), C1 (- - -).

The simulated sprays agree with experimental diameter measurements. The largest error is seen close to the burner, at $z = 10$ mm, where droplet diameters are underpredicted by 5 µm. A likely major contributor to this error is the lack of an atomization model in the simulations. The liquid phase is assumed to be fully atomized already at the point of injection, whereas, in reality, the fuel forms a film at the pre-filmer lip, which is then atomized by the air flow. The error may be reduced by directly modeling the film behavior or by forgoing the pre-filmer lip entirely and injecting the Lagrangian phase downstream of it. The lack of atomization model is likely also the reason why few to no droplets are observed in the simulations at $r < 5$ mm and $r > 22$ mm: the motions of the droplets are not chaotic enough to fling droplets very far inward or outward.

Another way to analyze the spray evolution is provided in Figure 13. The droplet diameter PDF for each fuel is plotted at six downstream locations, along with the initial Rosin–Rammler distribution used at injection. The end of the pre-filmer lip, and, thus, the beginning of the combustion chamber, is located at $z = 0$ mm. The smallest droplets evaporate fast in the surrounding air (650 K) due to their large diameter-to-volume ratio,

resulting in a decrease in small droplets along the pre-filmer lip. A substantial change takes place over the following 10 mm, where the fraction of small droplets ($d_p < 10$ µm) drops sharply, from 58% at $z = 0$ mm to 34% at $z = 5$ mm and 23% at $z = 10$ mm. The peak of the PDF is, thus, shifted to the right. Downstream of $z = 0$ mm, increasing temperatures accelerate the evaporation of larger droplets, reducing their size and flattening the PDF. As the last droplets evaporate between $z = 20$ mm and $z = 30$ mm, the data deteriorate. Thus, the notable differences that can be observed between Jet A and C1 at these locations should not be considered significant.

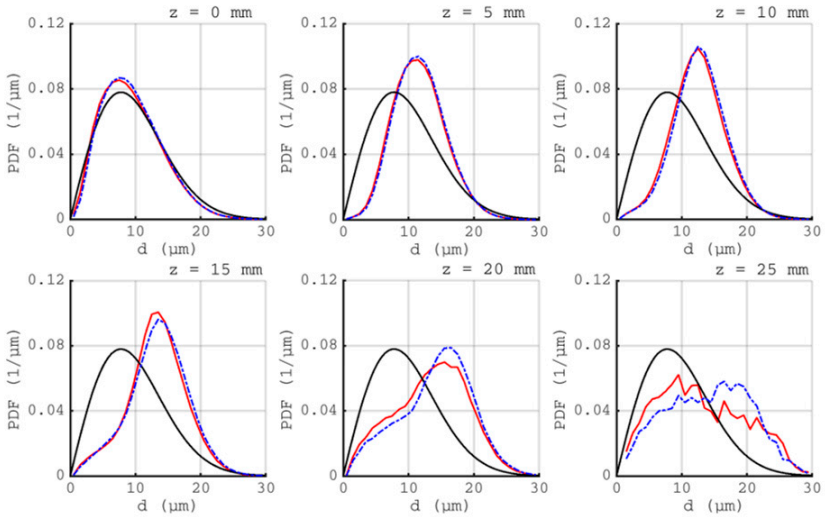

Figure 13. Probability density functions (PDF) of droplet diameter in six planes downstream of the burner. Black: PDF at injection. Legend: PDF at injection (—), Jet A (—), and C1 (- - -).

Upstream of $z = 20$ mm, where the number of droplets is large enough to construct reliable averages, it is evident in both Figures 12 and 13 that there are only minor differences between the Jet A spray and C1 spray. The most likely reason for this similarity is that identical liquid properties are used for both fuels. This includes specific heat capacity, enthalpy, vapor pressure, and viscosity. This choice was made to isolate the chemical reaction mechanism as the only decisive factor for the combustion process. Now that we have confirmed that both reaction mechanisms predict similar flames, which also resemble experimental observations, assigning accurate liquid properties to C1 will be a logical next step for future studies. Based on the findings in [62], Jet A and C1 should have non-negligible differences in density, viscosity, surface tension, and specific heat capacity, and it remains to be seen if and how much these properties will change the spray.

5.3. Helicopter Combustor

The computational domain of the third case here presented is represented by a ~26° sector of an annular reverse flow combustor inspired by the PT6C turboprop engine liner, often used for helicopters, such as the Augusta Westland 139 used by the Swedish Maritime Administration Search and Rescue. The selection of this specific geometrical configuration aims to eliminate the prospect of capturing thermoacoustic instabilities, which is out of the scope of this study. The liquid fuel is injected in the combustor, forming an injection angle of ~30° with respect to the *z*-axis, Figure 14a. The diameter of the droplets is based on the Rosin–Rammler distribution [84]. After the droplet vaporization, the gaseous fuel mixes with air and the resulting mixture starts to react in the primary sector of the combustor enclosed by the inner end wall and the dilution holes, Figure 14a. Within this combustor section, air is fed through a primary air film behind the injector, and primary holes at the lower wall of the combustor. Since the aim of this design is to decrease the pressure and increase the air flow velocity, as well as to reduce temperature and, consequently, the NO_X production [90,91], optimal combustion is achieved in two stages. Hence, additional air

enters the combustor through dilution jets (secondary holes in Figure 14a) and cooling films located at the inner wall on the return bend of the combustor. Here, LES-LDKM-EDC is performed on unstructured grids with ~5 million cells for both Jet A and C1 to characterize the differences between fossil and non-fossil fuels. Grids are clustered around primary and dilution holes, as well as inside the liner, with particular attention devoted to the grid size in the vicinity of the liner walls. As a result, on average, approximately 75% of the total turbulent kinetic energy belongs to the resolved scales. This fraction should typically be higher in LES, but it should be noted that it is brought down substantially by the large coarse-grained regions far from the region of interest, near the spray and flame. In said region of interest, over 99% of the turbulent kinetic energy is resolved. A projection of the baseline mesh on the wall and an outline of the domain is presented in Figure 14b.

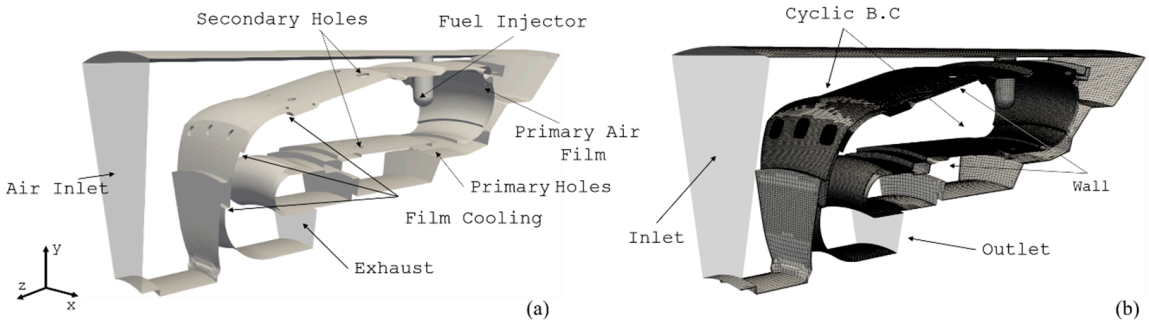

Figure 14. (**a**) Combustor components and (**b**) projection of the baseline grid on the combustor liner.

Dirichlet boundary conditions of the velocity, temperature, and pressure are used at the air inlet, whereas, at the outlet, variables are extrapolated, except for the pressure, which is subject to the wave-transmissive boundary condition [92]. Zero Dirichlet condition of the velocity and zero Neumann condition for all other variables are applied to the wall. To represent the influence of the neighboring, unresolved injectors, the Lagrangian particle cloud is tracked across the two lateral patches of the domain, imposing periodic boundary conditions. Based on the performances reported in [93], the combustor section used here is assumed to generate 1/14 of the take-off power (~431 kW). At this load, the engine performs with an overall pressure ratio of 6.3:1. Thus, the inlet air mass flow of 0.143 kg/s enters the computational domain with a temperature of 480 K and a pressure of 6.3 bar. To achieve the aforementioned maximum power, each nozzle injects liquid fuel with an overall flow rate of 0.049 kg/s. Based on [94], the injection pressure during the take-off varies between 31 and 41 bar, and, hence, the injector nozzle size has been modeled with injection speed equal to 50 m/s. The injection speed was extrapolated from results presented in [95], while the spray half-cone angle was set to 60° based on [96]. Table 2 summarizes the operating conditions considered.

Table 2. Key parameters of the helicopter engine LES.

Inlet Air Velocity (m/s)	10.2
Inlet Air Temperature (K)	490
Fuel Mass Rate (kg/s)	0.04885
Injection Speed (m/s)	50.0

Figure 15a presents instantaneous volumetric renderings of the temperature, *T*, for C1. The inlet air enters from the back of the liner through the multiple holes, allowing the spray to vaporize and the gaseous fuel to mix with the air. A volumetric rendering of the temperature field suggests that the combustion process mainly occurs between the primary and secondary air holes, the role of which is to create a high-strain region inside the liner able (i) to recirculate fuel and air, as well as hot radicals, and (ii) to stabilize the flame. Similar behavior has been shown on a similar architecture studied by Boudier et al. [97].

Furthermore, the extra air entrainment into the liner through the cooling air films and holes drastically reduces the combustion products' temperature, confining the hot gases at the inner part of the liner. Figure 15b presents the overall functioning of the chamber through an instantaneous perspective view of the velocity magnitude, U, on a lateral patch, the projection of the temperature, T, on the outlet, the C1 Lagrangian field colored in magenta, and a volumetric rendering of heat release rate, Q. Concerning the projection of the velocity field, it is visible how the mesh resolution captures the flow structures formed by the spreading of fresh air in the inner combustion chamber well, highlighting the complexity of the resulting flow field. The fuel droplet locations, as well as the distribution of the rate of heat release, suggest that the liquid fuel evaporates mainly through interaction with the air coming from the primary film and primary holes, while the combustion process proceeds in the region between the primary and the secondary holes. The reacting mixture and combustion products are accelerated toward the outlet by the reversed combustor configuration. The temperature at the outlet also shows the effect of the cooling films shielding the liner from the hot combustion products.

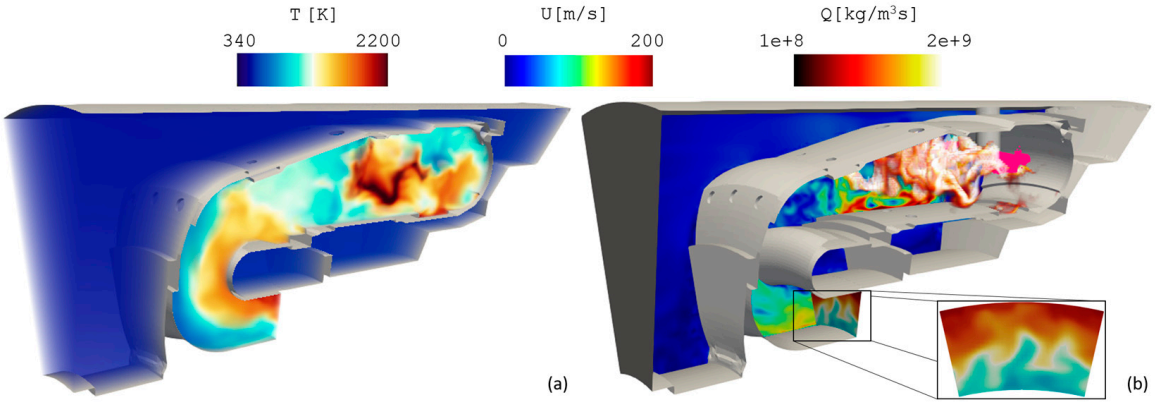

Figure 15. (**a**) Volumetric rendering of the instantaneous temperature in the combustor for C1 and (**b**) instantaneous velocity magnitude, U, on the cyclic patch and the temperature, T, on the outlet; instantaneous volumetric rendering of the heat release, Q, and spray (magenta).

Figure 16 presents a time-sequence of the spray colored by the droplet diameter. Cyclic boundary conditions allow the droplets to leave the sector once they reach the right-side patch and to re-enter the combustor through the left-side patch. The droplet time sequence highlights how the liquid fuel is kept confined at the upstream part of the combustor by the flow and how the droplet diameter decreases due to vaporization.

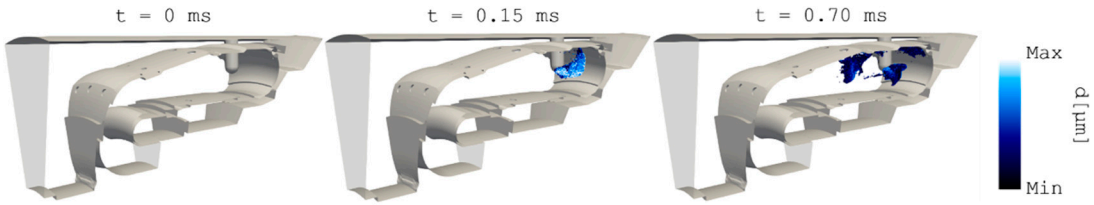

Figure 16. Sequence of snapshots of the Lagrangian particle cloud after the start of injection. The Lagrangian particle cloud is colored by the diameter, d_p.

Figure 17 presents volumetric renderings of (a) vaporized fuel, C1, short-term combustion radicals, C_2H_4 and HCO, and (b) major species related to the combustion process OH, CO, and CO_2. The distribution of $\widetilde{Y}_{C1}$ highlights how the air from the primary holes at the lower liner wall confines the vaporized fuel to the upper part of the upstream combustor section. The fuel breakdown products, e.g., C_2H_4, and various intermediate species, such as HCO, form downstream of the vaporized fuel cloud, facilitating a two-stage burning

process, whereby CO is formed in the upstream part of the combustor and CO_2 in the downstream part of the combustor. Figure 17b shows that OH is formed around the region of C1, C_2H_4, and HCO and that CO and CO_2 occur along the combustor in a sequential manner: First, CO is formed primarily at the upstream part of the combustor, where vaporized fuel and hot air and combustion products mix and react under rich conditions. Downstream of the CO-rich zone, OH dominates the region between the primary and the secondary holes, in which also the spray is injected and where much of the heat release occurs. Downstream of the OH-rich zone, additional oxygen enters the combustor through the primary and secondary holes, and gradually lean combustion conditions are obtained, resulting in the conversion of CO to CO_2 and, thus, completing the combustion process. This two-stage combustion process facilitates low NO_X emissions through the rich–lean sequence and further dilutes the combustion products by cold air from the film cooling holes in the far downstream part of the combustor and towards the exhaust section.

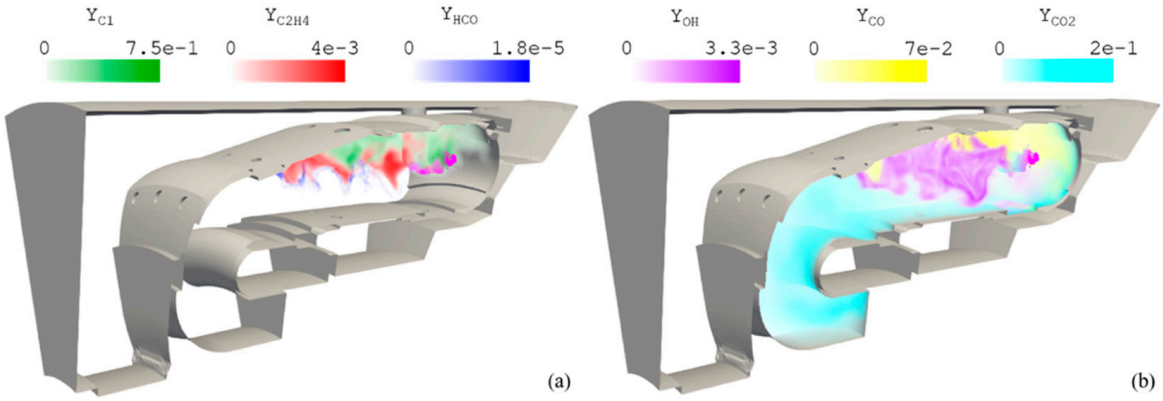

Figure 17. Instantaneous spray distribution (in magenta), together with volumetric renderings of (**a**) C1, C_2H_4, and HCO and (**b**) OH, CO, and CO_2.

To further characterize the evolution of the spray cloud, the mean radial profiles of the droplet diameter and the corresponding radial temperatures are shown in Figure 18. Results refer to three different planes located downstream of the injector nozzle along the direction of injection, ζ, assuming positive and negative the two sides in front of and behind the injector, respectively. Thus, negative values of ζ are related to statistics over droplets that have re-entered the domain through the left-side cyclic path. The diameters in Figure 18 follow qualitatively the temperature distribution, with the largest particles associated with the highest spray droplet temperatures. The spatial distribution of d_p can be explained by imagining the relatively hot gas surrounding the spray cloud enhancing the vaporization of the smallest droplets at the edge of the spray cloud, while the higher thermal inertia of the biggest droplets delays their evaporation. Thus, similarly to what has been shown in Section 5.2, the inner- and outermost droplets have the highest diameters, as they are subjected to the most intense heating. This is not visible at $r = 0$ mm and at $\zeta = 10$ mm, where the temperature increases along the radial direction. Reasonably, the edges of the particle distribution are not uniformly heated yet, since only the particles at large radii are exposed to the high temperatures of the combustion chamber. The spatial distribution of d_p at $\zeta = -30$ mm suggests that, far downstream of the injector location, the spray cloud is quite confined between 10 mm $< r <$ 20 mm. Furthermore, there exists a discontinuity along the radial direction between $r = 15$ mm and $r = 25$ mm. This result suggests that the complexity of the flow forces some of the particles (reasonably the ones at the borders of the droplet distribution) to leave the main droplet cloud and to form isolated clouds. Although the trends differ slightly locally, no significant differences can be noted between the fossil and non-fossil jet fuels.

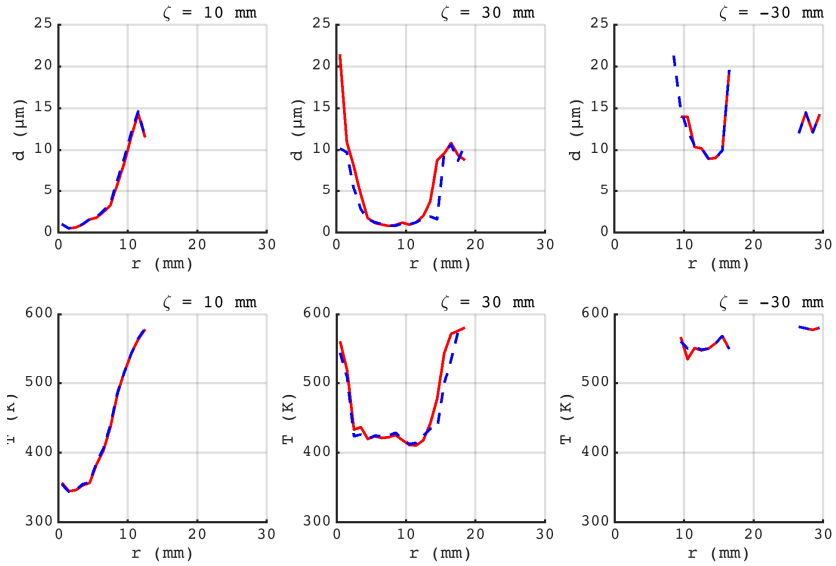

Figure 18. Radial distributions of time-averaged diameter (**top**) and temperature (**bottom**) at three different locations along the direction of injection. Negative values of ζ refer to spray sections upstream the injector. Legend: Jet A (—) and C1 (-·-·-).

Figure 19 shows the droplet diameter PDF for Jet A and C1 at three locations downstream of the spray nozzle (top row) and three locations upstream (bottom row). The Rosin–Rammler distribution at the injection section has been added for comparison. PDFs show how, below $\zeta = -30$ mm, Jet A and C1 distributions are similar and do not differ much from the initial Rosin–Rammler distribution. However, the rate of change of the biggest particle PDF profiles is relevant when comparing different spatial locations. In fact, it is visible how the droplet population around $d_p = 20$ µm progressively decreases from $\zeta = 10$ mm to $\zeta = 30$ mm. Hence, the vaporization process increases the population around the peak (at $d_p \approx 7.5$ µm) by 17.32 % from $\zeta = 10$ mm to $\zeta = 30$ mm for the two different fuels. In addition, the fuel vaporization at diameters smaller than 7.5 µm is then compensated by a progressive shrinkage of larger droplets. A substantial change takes place on sampling planes located at negative ζ. In fact, the longer exposure to the hot gases from the surrounding combustion accelerates the vaporization of the small droplets, shifting the PDF peaks to the right. Similar to the DLR burner, only minor differences are visible between Jet A and C1 due to the same liquid fuel properties being used in the simulations.

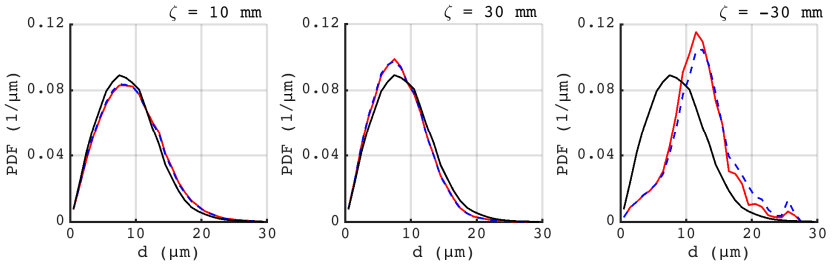

Figure 19. Probability density functions (PDF) of droplet diameter in six planes downstream of the injector nozzle. Negative values of ζ refer to spray sections upstream of the injector. Legend: PDF at injection (—), Jet A (—), C1 (-·-·-).

6. Concluding Remarks

The combustion of various jet fuels was investigated numerically using large eddy simulations with fine rate chemistry, targeting three different combustors: a premixed bluff body burner, a laboratory single-cup swirl-stabilized spray combustor, and a single-

sector model helicopter engine with spray injection. Simulations were carried out using conventional Jet A and a synthetic jet fuel, C1. In addition, n-dodecane was also investigated but only in the premixed case. The main findings of this study can be summarized as:

For the premixed bluff-body burner, LES with finite-rate chemistry showed improved qualitative agreement over a flame surface density model. This motivated using the finite-rate chemistry LES model for the subsequent spray simulations. Only small differences between n-dodecane, Jet A, and C1 were observed in the $\langle \widetilde{v}_x \rangle$, $\langle \widetilde{T} \rangle$, and $\langle \widetilde{Y}_i \rangle$, profiles, with n-dodecane showing the highest velocity, temperature, and pressure fluctuations.

For the single-cup swirl-stabilized spray combustor, Jet A and C1 were found to produce similar flames, with Jet A showing good agreement with the experimental data. Based on the Takeno Flame Index, the flames were found to burn in a premixed mode. The droplet size distribution in the case of Jet A resembled experimental observations at 15 and 20 mm downstream of the pre-filmer lip but was underpredicted further upstream. This difference was due to the lack of an atomization model capable of capturing the spray formation at the end of the pre-filmer lip. The peak droplet temperatures were found at the inner and outer edges of the spray, following the heating from the inner and outer recirculation zones.

For the helicopter engine, combustion proceeded as a two-stage combustion process consisting of a vaporization stage, followed by a main combustion stage. Evaporation occurred mainly through interaction between the fuel and the air coming from the primary film and primary air holes at the back of the liner, while combustion mainly occurred between the primary and secondary air holes. As with the single-cup combustor, peak temperatures were observed at the edges of the spray, with a clear correlation between temperature and droplet diameter caused by the higher thermal inertia of large droplets compared to small droplets. This higher thermal inertia also caused the peak of the droplet diameter probability distribution to shift towards higher diameters during the evolution of the spray. The results obtained for Jet A were very similar to those obtained for C1; future simulations will show if this behavior persists if the thermophysical properties of the dispersed phase are altered to match Jet A and C1 specifically.

Author Contributions: Conceptualization, C.F.; methodology, A.Å., F.P. and C.F.; investigation, A.Å., F.P. and C.F.; resources, C.F.; writing—original draft preparation, A.Å., F.P. and C.F.; writing—review and editing, A.Å., F.P. and C.F.; visualization, A.Å., F.P. and C.F.; project administration, C.F.; funding acquisition, C.F. All authors have read and agreed to the published version of the manuscript.

Funding: This work was supported by the European Union's Horizon 2020 research and innovation program MORE&LESS under grant agreement no. 769246, the competence center CESTAP funded by the Swedish Energy Agency, Industry and Academia in collaboration, as well as the projects Fossil free SAR Helicopters 2045—A pilot study and Numerical studies of performance variations in the combustion of 100% biojet fuel in a jet engine, both funded by the Swedish Energy Agency. Computer time was partly provided by the Swedish National Infrastructure for Computing, partially funded by the Swedish Research Council through grant agreement no. 2018-05973.

Institutional Review Board Statement: Not applicable.

Informed Consent Statement: Not applicable.

Data Availability Statement: Data supporting the findings of this study are available from the corresponding author upon reasonable request.

Acknowledgments: The authors acknowledge Martin Passad and Elna Heimdal Nilsson for their insight and aid on the chemical kinetics and extinction strain rate in particular.

Conflicts of Interest: The authors declare no conflict of interest.

References

1. Harrison, R.M.; Maisol, M.; Vardoulakis, S. Civil Aviation, Air Pollution and Human Health. *Environ. Res. Lett.* **2015**, *10*, 41001. [CrossRef]
2. Kärcher, B. Aviation Produced Aerosols and Contrails. *Surv. Geophys.* **1999**, *20*, 113. [CrossRef]
3. Lee, D.S.; Fahey, D.W.; Skowron, A.; Allen, M.R.; Burkhardt, U.; Chen, Q.; Doherty, S.J.; Freeman, S.; Forster, P.M.; Fuglestvedt, J.; et al. The Contribution of Global Aviation to Anthropogenic Climate Forcing for 2000 to 2018, 2021. *Atm. Environ.* **2021**, *244*, 117834. [CrossRef] [PubMed]
4. *Standard D1655*; Standard Specification for Aviation Turbine Fuels. ASTM: West Conshohocken, PA, USA, 2022.
5. Kumar, K.; Sung, C.-J. An Experimental Study of the Autoignition Characteristics of Conventional Jet Fuel/Oxidizer Mixtures: Jet-A and JP-8. *Comb. Flame* **2010**, *157*, 676. [CrossRef]
6. Blakely, S.; Rye, L.; Wilson, C.W. Aviation Gas Turbine Alternative Fuels: A. Review. *Proc. Comb. Inst.* **2011**, *33*, 2863. [CrossRef]
7. Braun-Unkhoff, M.; Riedel, U. Alternative Fuels in Aviation. *CEAS Aeronaut. J.* **2015**, *6*, 83. [CrossRef]
8. Yang, J.; Xin, Z.; Quan, H.; Corscadden, K.; Niu, H. An Overview on Performance Characteristics of Bio-Jet Fuels. *Fuel* **2019**, *237*, 916. [CrossRef]
9. Kick, T.; Herbst, J.; Kathrodia, T.; Marquetand, J.; Braun-Unkhoff, M.; Riedel, U. An Experimental and Modeling Study of Burning Velocities of Possible Future Synthetic Jet Fuels. *Energy* **2012**, *43*, 111. [CrossRef]
10. Zhang, C.; Hui, X.; Lin, Y.; Sung, C.-J. Recent Development in Studies of Alternative Jet Fuel Combustion: Progress, Challenges, and Opportunities. *Ren. Sust. Energy Rev.* **2016**, *54*, 120. [CrossRef]
11. Available online: https://www.icao.int/environmental-protetion/GFAAF/Pages/Conversion-processes.aspx (accessed on 13 October 2022).
12. Available online: https://web.stanford.edu/group/haiwanglab/HyChem/fuels/C1_spec.html (accessed on 13 October 2022).
13. Echekki, T.; Mastorakos, E. *Turbulent Combustion Modeling, Fluid Mechanics and its Applications*; Springer Science + Business Media: Berlin, Germany, 2011; Volume 95.
14. Menon, S.; Fureby, C. Computational Combustion. In *Encyclopedia of Aerospace Engineering*; Blockley, R., Shyy, W., Eds.; John Wiley & Sons: Hoboken, NJ, USA, 2010.
15. Faeth, G.M. Mixing, Transport and Combustion in Sprays. *Prog. Energy Comb. Sci.* **1987**, *13*, 293. [CrossRef]
16. Giacomazzi, E.; Picchia, F.R.; Arcidiacono, N. On the Distribution of Lewis and Schmidt Numbers in Turbulent Flames. In Proceedings of the 30th Event of the Italian Section of the Combustion Institute, Ischia, Italy, 20–23 June 2007.
17. Sagaut, P. *Large Eddy Simulation for Incompressible Flows*; Springer Verlag: Berlin/Heidelberg, Germany, 2001.
18. Smagorinsky, J. General Circulation Experiments with the Primitive Equations. *Mon. Weather. Rev.* **1963**, *91*, 99. [CrossRef]
19. Germano, M.; Piomelli, U.; Moin, P.; Cabot, W. A Dynamic Subgrid-Scale Eddy Viscosity Model. *Phys. Fluids A* **1991**, *3*, 1760. [CrossRef]
20. Yoshizawa, A. A Statistically-derived Subgrid-scale Kinetic Energy Model for the Large Eddy Simulation of Turbulent Flows. *J. Phys. Soc. Jpn.* **1985**, *54*, 2834. [CrossRef]
21. Kim, W.-W.; Menon, S. A New Dynamic One Equation Subgrid-scale Model for Large Eddy Simulations. In Proceedings of the 19th Aerospace Sciences Meeting, Reno, NV, USA, 9–12 January 1995. AIAA 95-0356.
22. Wang, Z.J.; Li, Y. A Mathematical Analysis of Scale Similarity. *Com. Comp. Phys.* **2017**, *21*, 149. [CrossRef]
23. Cook, A.W.; Riley, J.J. A Subgrid Model for Equilibrium Chemistry in Turbulent Flows. *Phys. Fluids* **1994**, *6*, 2868. [CrossRef]
24. Branley, N.; Jones, W.P. Large Eddy Simulation of a Turbulent Non-Premixed Flame. *Comb. Flame* **2001**, *127*, 1914. [CrossRef]
25. Peters, N. *Turbulent Combustion*; Cambridge University Press: Cambridge, UK, 2000.
26. Fureby, C. Large Eddy Simulation of Combustion Instabilities in a Jet-Engine Afterburner Model. *Comb. Sci. Technol.* **2000**, *161*, 213. [CrossRef]
27. Hawkes, E.R.; Cant, R.S. Implications of a Flame Surface Density Approach to Large Eddy Simulation of Premixed Turbulent Combustion. *Comb. Flame* **2001**, *126*, 1617. [CrossRef]
28. Weller, H.G.; Tabor, G.; Gosman, A.D.; Fureby, C. Application of a Flame-Wrinkling LES Combustion Model to a Turbulent Shear Layer Formed at a Rearward Facing Step. *Proc. Comb. Inst.* **1998**, *27*, 899. [CrossRef]
29. Veynante, D. Investigation of Flame Surface Density Modeling for Large Eddy Simulation of Turbulent Premixed Flames by Comparison with a Prescribed Reference Solution. *Comb. Flame* **2022**, *239*, 111663. [CrossRef]
30. Bai, X.-S.; Fureby, C. Non-Premixed and Partially Premixed Combustion. In *Turbulent Combustion*; Swaminathan, N., Bai, X.-S., Brethouwer, G., Haugen, N.E.L., Fureby, C., Eds.; Cambridge University Press: Cambridge, UK, 2019; p. 162.
31. Ma, T.; Stein, O.T.; Chakraborty, N.; Kempf, A. A Posteriori Testing of Algebraic Flame Surface Density Models for LES. *Comb. Theory Model.* **2013**, *17*, 431. [CrossRef]
32. Colin, O.; Ducros, F.; Veynante, D.; Poinsot, T. A Thickened Flame Model for Large Eddy Simulation of Turbulent Premixed Combustion. *Phys. Fluids.* **2000**, *12*, 1843. [CrossRef]
33. Fureby, C. LES Modeling of Combustion for Propulsion Applications. *Phil. Trans. R. Soc. A* **2009**, *367*, 2957. [CrossRef] [PubMed]
34. Giacomazzi, E.; Bruno, C.; Favini, B. Fractal Modeling of Turbulent Combustion. *Comb. Theory Model.* **2000**, *4*, 391. [CrossRef]
35. Sabelnikov, V.; Fureby, C. LES Combustion Modeling for High Re Flames using a Multi-phase Analogy. *Comb. Flame* **2013**, *160*, 83. [CrossRef]

36. Jones, W.P.; Marquis, A.-J.; Wang, F. Large Eddy Simulation of a Premixed Propane Turbulent Bluff Body Flame using the Eulerian Stochastic Field Method. *Fuel* **2015**, *140*, 514. [CrossRef]
37. Menon, S. Subgrid Combustion Modeling for Large Eddy Simulations. *Int. J. Engine Res.* **2000**, *1*, 209. [CrossRef]
38. Bulat, G.; Fedina, E.; Fureby, C.; Meier, W.; Stopper, U. Reacting Flow in an Industrial Gas Turbine Combustor: LES and Experimental Analysis. *Proc. Comb. Inst.* **2014**, *35*, 3175. [CrossRef]
39. Nilsson, T.; Zhong, S.; Fureby, C. LES of H_2-air Jet Combustion in High Enthalpy Supersonic Crossflow. *Phys. Fluids* **2021**, *33*, 35133. [CrossRef]
40. Magnussen, B.F. On the Structure of Turbulence and Generalized Eddy Dissipation Concept for Chemical Reactions in Turbulent Flow. In Proceedings of the 19th Aerospace Sciences Meeting, St. Louis, MO, USA, 12–15 January 1981. AIAA 1981-0042.
41. Chomiak, J. A Possible Propagation Mechanism of Turbulent Flames at High Reynolds Numbers. *Comb. Flame* **1970**, *15*, 319. [CrossRef]
42. Batchelor, G.K.; Townsend, A.A. The Nature of Turbulent Motion at Large Wave-numbers. *Proc. Roy. Soc. London A* **1949**, *199*, 238.
43. Dukowicz, J.K. A Particle-Fluid Numerical Model for Liquid Sprays. *J. Comp. Phys.* **1980**, *35*, 229. [CrossRef]
44. Apte, S.V.; Goroskhovski, M.; Moin, P. LES of Atomizing Spray with Stochastic Modeling of Secondary Breakup. *Int. J. Multiph. Flow* **2003**, *29*, 1503. [CrossRef]
45. Faeth, G.M. Evaporation and Combustion of Sprays. *Prog. Energy Comb. Sci.* **1983**, *9*, 1. [CrossRef]
46. Faeth, G.M. Spray Combustion Phenomena. *Proc. Comb. Inst.* **1996**, *26*, 1593. [CrossRef]
47. Reitz, R.D. Mechanisms of Atomization Processes in High-Pressure Vaporizing Sprays. *At. Spray Technol.* **1987**, *3*, 309.
48. Reitz, R.D.; Diwakar, R. Effect of Drop Breakup on Fuel Sprays. *SAE Technol. Pap.* **1986**, *95*, 860469.
49. Crowe, C.T.; Sommerfeld, M.; Tsuji, Y. *Multiphase Flows with Droplets and Particles*; CRC Press LLC: Boca Raton, FL, USA, 1998.
50. Ranz, W.E.; Marshall, W.R. Evaporation from Drops. *Chem. Eng. Prog.* **1952**, *48*, 141.
51. Weller, H.G.; Tabor, G.; Jasak, H.; Fureby, C. A Tensorial Approach to CFD using Object Oriented Techniques. *Comp. Phys.* **1997**, *12*, 620. [CrossRef]
52. Lambert, J.D. *Computational Methods in Ordinary Differential Equations*; John Wiley & Sons Inc.: Hoboken, NJ, USA, 1973.
53. Issa, R.I. Solution of the Implicitly Discretized Fluid Flow Equations by Operator Splitting. *J. Comp. Phys.* **1986**, *62*, 40. [CrossRef]
54. Strang, G. On the Construction and Comparison of Difference Schemes. *SIAM J. Numer. Anal.* **1968**, 506. [CrossRef]
55. Rosenbrock, H.H. Some General Implicit Processes for the Numerical Solution of Differential Equations. *Comput. J.* **1963**, *5*, 329. [CrossRef]
56. Hairer, E.; Wanner, G. *Solving Ordinary Differential Equations II Stiff and Differential-Algebraic Problems*, 2nd ed.; Springer: Berlin/Heidelberg, Germany, 1991.
57. *Handbook of Aviation Fuels, Society of Automotive Engineers*; Report No. 635; Coordinating Research Council, SAE: Alpharetta, GA, USA, 2004.
58. Maurice, L.Q.; Lander, H.; Edwards, T.; Harrison, W.E. Advanced Aviation Fuels: A Look Ahead via a Historical Perspective. *Fuel* **2001**, *80*, 747. [CrossRef]
59. Bowden, J.N.; Westbrook, S.R.; LePera, M.E. Jet Kerosene Fuels for Military Diesel Application, SAE Transactions. *J. Fuels Lubr.* **1989**, *98*, 810.
60. Aicholtz, J.; Holland, T.; Andac, G.; Boehm, R.; Seto, S.; Lewis, R.; Williams, R.; Ludwig, D.; James, S.; Mosbacher, M.; et al. Development of Combustion Rules and Tools for the Characterization of Alternative Fuels. AFRL-RZ-WP-TR-2010-2134 MACCCR 3rd Annual Fuels Summit Princeton, NJ, 20 September 2010. Available online: https://kinetics.nist.gov/RealFuels/macccr/macccr2010/MACCCR_2010_Colket.pdf (accessed on 13 October 2022).
61. Colket, M.; Heyne, J.; Rumizen, M.; Gupta, M.; Edwards, T.; Roquemore, W.M.; Andac, R.; Boehm, R.; Lovett, J.; Williams, R.; et al. Overview of the National Jet Fuels Combustion Program. *AIAA J.* **2017**, *55*, 1087. [CrossRef]
62. Edwards, T. Reference Jet Fuels for Combustion Testing. In Proceedings of the 55th AIAA Aerospace Sciences Meeting, Grapevine, TA, USA, 9–13 January 2017. AIAA 2017-0146.
63. Yao, T.; Pei, Y.; Zhong, B.-J.; Som, S.; Lu, T.; Luo, K.H. A Compact Skeletal Mechanism for n-dodecane with Optimized Semi-Global Low-Temperature Chemistry for Diesel Engine Simulations. *Fuel* **2017**, *191*, 339. [CrossRef]
64. Wang, H.; Xu, R.; Wang, K.; Bowman, C.T.; Davidson, D.F.; Hanson, R.K.; Brezinsky, K.; Egolfopoulos, F.N. A Physics-Based Approach to Modeling Real-Fuel Combustion Chemistry—I. Evidence from Experiments, and Thermodynamic, Chemical Kinetic and Statistical Considerations. *Comb. Flame* **2018**, *193*, 502. [CrossRef]
65. Kumar, K.; Sung, C.-J. Laminar Flame Speeds and Extinction Limits of Preheated n-decane/O_2/N_2 and n-dodecane/O_2/N_2 Mixtures. *Comb. Flame* **2007**, *151*, 209. [CrossRef]
66. Xu, R.; Wang, K.; Banerjee, S.; Shao, J.; Parise, T.; Zhu, Y.; Wang, S.; Movaghar, A.; Lee, D.J.; Zhao, R.; et al. A Physics-Based Approach to Modeling Real-Fuel Combustion Chemistry—II. Reaction Kinetic Models of Jet and Rocket Fuels. *Comb. Flame* **2018**, *193*, 520. [CrossRef]
67. Dooley, S.; Hee Won, S.; Heyne, J.; Farouk, T.; Ju, Y.; Dryer, F.; Kumar, K.; Hui, X.; Sung, C.-J.; Wang, H.; et al. The Experimental Evaluation of a Methodology for Surrogate Fuel Formulation to Emulate Gas Phase Combustion Kinetic Phenomena. *Comb. Flame* **2012**, *159*, 1444. [CrossRef]
68. Hui, X.; Sung, C.-J. Laminar Flame Speeds of Transportation-relevant Hydrocarbons and Jet Fuels at Elevated Temperatures and Pressures. *Fuel* **2013**, *109*, 191. [CrossRef]

69. Kumar, K.; Sung, C.-J.; Hui, X. Laminar Flame Speeds and Extinction Limits of Conventional and Alternative Jet Fuels. *Fuel* **2011**, *90*, 1004. [CrossRef]
70. Liu, S.; Zhao, R.; Xu, R.; Egolfopoulos, F.N.; Wang, H. Binary Diffusion Coefficients and Non-premixed Flames Extinction of Long-chain Alkanes. *Proc. Comb. Inst.* **2017**, *36*, 1523. [CrossRef]
71. Mao, Y.; Raza, M.; Wu, Z.; Zhu, J.; Yu, L.; Wang, S.; Zhu, L.; Lu, X. An Experimental Study of n-dodecane and the Development of an Improved Kinetic Model. *Comb. Flame* **2020**, *212*, 388. [CrossRef]
72. *Ansys Chemkin-Pro*; Ansys Inc.: Canonsburg, PA, USA, 2016.
73. Paxton, B.T.; Fugger, C.A.; Tomlin, A.S.; Caswell, A.W. Experimental Investigation of Fuel Type on Combustion Instabilities in a Premixed Bluff- Body Combusto. In Proceedings of the AIAA Scitech 2020 Forum, Orlando, FL, USA, 6–10 January 2020. AIAA 2020-0174.
74. Fugger, C.A.; Yi, T.; Sykes, J.P.; Rankin, B.; Miller, J.D.; Gord, J.R. The Structure and Dynamics of a Bluff-Body Stabilized Premixed Reacting Flow. In Proceedings of the 2018 AIAA Aerospace Sciences Meeting, Kissimmee, FL, USA, 8–12 January 2018. AIAA 2018-1190.
75. Fugger, C.A.; Roy, S.; Caswell, A.W.; Rankin, B.; Gord, J.R. Structure and Dynamics of CH2O, OH, and the Velocity Field of a Confined Bluff-body Premixed Flame, using Simultaneous PLIF and PIV at 10 kHz. *Proc. Comb. Inst.* **2019**, *37*, 1461. [CrossRef]
76. Sjunesson, A.; Nelson, C.; Max, E. *LDA Measurements of Velocities and Turbulence in a Bluff Body Stabilized Flame*; Aero Technical Report S-461 81; Volvo: Gothenburg, Sweden, 1991.
77. Sjunesson, A.; Henriksson, R.; Löfström, C. CARS Measurements and Visualization of Reacting Flows in Bluff Body Stabilized Flame. In Proceedings of the 28th Joint Propulsion Conference and Exhibit, Nashville, TN, USA, 6–8 July 1992. AIAA 1992–3650.
78. Fureby, C. The Volvo Validation Rig—A Comparative Study of Large Eddy Simulation Combustion Models at Different Operating Conditions. In Proceedings of the 2018 AIAA Aerospace Sciences Meeting, Kissimmee, FL, USA, 8–12 January. AIAA 2018–0149.
79. Fureby, C. A Large Eddy Simulation (LES) Study of the VOLVO and AFRL Bluff Body Combustors at Different Operating Conditions. In Proceedings of the AIAA Scitech 2019 Forum, San Diego, CA, USA, 7–11 January 2019. AIAA 2019-0453.
80. Erickson, R.R.; Soteriou, M.C.; Mehta, P.G. The Influence of Temperature Ratio on the Dynamics of the Bluff Body Stabilized Flames. In Proceedings of the 12th AIAA/CEAS Aeroacoustics Conference (27th AIAA Aeroacoustics Conference), Cambridge, MA, USA, 8–10 May 2006. AIAA 2006-0753.
81. Ehn, A. Towards Quantitative Diagnostics using Short-Pulse Laser Techniques. Ph.D. Thesis, Division of Combustion Physics, Faculty of Engineering, Lund University, Lund, Sweden, 2012.
82. Behrendt, T.; Frodermann, M.; Hassa, C.; Heinze, J.; Lehmann, B.; Stursberg, K. Optical Measurements of Spray Combustion in a Single Sector Combustor from a Practical Fuel Injector at Higher Pressures. In Proceedings of the Symposium on Gas Turbine Engine Combustion, Emissions and Alternative Fuels, Lisboa, Portugal, 12–16 October 1999.
83. Meier, U.; Heinze, J.; Freitag, S.; Hassa, C. Spray and Flame Structure of a Generic Injector at Aero-engine Conditions. *J. Eng. Gas Turbines Power* **2012**, *134*, 31503. [CrossRef]
84. Jones, W.P.; Marquis, A.J.; Vogiatzaki, K. Large-Eddy Simulation of Spray Combustion in a Gas Turbine Combustor. *Comb. Flame* **2014**, *161*, 222. [CrossRef]
85. Andreini, A.; Bertini, D.; Mazzei, L.; Puggelli, S. Assessment of a Numerical Procedure for Scale Resolved Simulations of Turbulent Spray Flames. In Proceedings of the XXXIX Meeting of the Italian Section of the Combustion Institute, Naples, Italy, 4–6 July 2016.
86. Puggelli, S.; Paccati, S.; Bertini, D.; Mazzei, L.; Giusti, A.; Andreini, A. Multi-coupled Numerical Simulations of the DLR Generic Single Sector Combustor. *Comb. Sci. Technol.* **2018**, *190*, 1409. [CrossRef]
87. Åkerblom, A. The Impact of Reaction Mechanism Complexity in LES of Liquid Kerosene Spray Combustion. In Proceedings of the 33rd Congress of the International Council of the Aeronautical Sciences, Stockholm, Sweden, 4–9 September 2022.
88. Von Kármán, T. Mechanische Ähnlichkeit und Turbulenz, Nachrichten von der Gesellschaft der Wissenschaften zu Göttingen, Fachgruppe 1. *Mathematik* **1930**, *5*, 58.
89. Yamashita, H.; Shimada, M.; Takeno, T. A Numerical Study on Flame Stability at the Transition Point of Jet Diffusion Flames. *Proc. Comb. Inst.* **1996**, *26*, 27. [CrossRef]
90. *PT6—Descriptive Course and Guide to Troubleshooting*; United Turbine Corp.: MIAMI, FL, USA, 2022.
91. Boudier, G.; Gicquel, L.Y.M.; Poinsot, T.J. Effects of Mesh Resolution on Large Eddy Simulation of Reacting Flows in Complex Geometry Combustors. *Comb. Flame* **2008**, *155*, 196. [CrossRef]
92. Poinsot, T.J.; Lele, S.K. Boundary Conditions for Direct Simulations of Compressible Viscous Flows. *J. Comp. Phys.* **1992**, *101*, 104. [CrossRef]
93. Taylor, J.W.R. *Jane's All the World's Aircraft 1962–63*; McGraw-Hill Book Company: New York, NY, USA, 1962.
94. Available online: https://www.aviationpros.com/home/article/10381485/pt6-fuel-nozzles (accessed on 13 October 2022).
95. Sivathanu, Y.; Lim, J.; Muliadi, A.; Nitulescu, O.; Shieh, T. Estimating Velocity in Gasoline Direct Injection Sprays using Statistical Pattern Imaging Velocimetry. *Int. J. Spray and Comb. Dyn.* **2019**, *11*, 1. [CrossRef]
96. Ballal, D.R.; Lefebvre, A.H. *Gas Turbine Combustion: Alternative Fuels and Emissions*, 3rd ed.; CRC Press: Boca Raton, FL, USA, 2010.
97. Boudier, G.; Gicquel, L.Y.M.; Poinsot, T.J.; Bissières, D.; Bérat, C. Comparison of LES, RANS and Experiments in an Aeronautical Gas Turbine Combustion Chamber. *Proc. Comb. Inst.* **2007**, *31*, 3075. [CrossRef]